# Scaling of Ultrafast Photon-Triggered Field Emission Cathodes Composed of Arrays of Sharpened Single-Crystal Si Pillars

By

Chen Dan Dong

S.B., Electrical Engineering, Applied Math, M.I.T., 2013

Submitted to the Department of Electrical Engineering and Computer Science
in Partial Fulfillment of the Requirements for the Degree of
Master of Engineering in Electrical Engineering and Computer Science
at the

Massachusetts Institute of Technology
September 2014

Author: Signature redacted

Department of Electrical Engineering and Computer Science
August 27, 2014

Certified by: Signature redacted

Dr. Luis Fernando Velásquez-García, Principal Research Scientist,
Thesis Supervisor
August 27, 2014

Accepted by: Signature redacted

Prof. Albert R. Meyer,
Chairman,
Masters of Engineering Thesis Committee

# Scaling of Ultrafast Photon-Triggered Field Emission Cathodes Composed of Arrays of Sharpened Single-Crystal Si Pillars

By

Chen Dan Dong

Submitted to the

Department of Electrical Engineering and Computer Science

September, 2014

In Partial Fulfillment of the Requirements for the Degree of

Master of Engineering in Electrical Engineering and Computer Science

## Abstract

Ultrafast (<1ps-long pulses) cathodes with spatially structured emission are an enabling technology for exciting applications such as free-electron lasers, tabletop coherent x-ray sources, and ultrafast imaging. In this thesis, we explore the scaling down and multiplexing limits of ultrafast photon-triggered field emission cathodes composed of arrays of nano-sharp high-aspect-ratio silicon pillars. We are interested in exploring how the geometry of the array and the morphology of the pillars affect the emission of the electrons. Both the multi-photon regime and the strong-field tunneling regime of the emission process were studied using near-IR pulses at various pulse energies. We model the structure using 2D and 3D COMSOL Multiphysics, collect the charge-energy characteristics of the actual devices, compare and interpret the results from both simulations and experiments. We find that the field factor is a strictly increasing function of the pitch at the fixed height, and the field factor saturates when the pitch is very large. The field factor is also strictly increasing with respect to the height with a diminishing return. In addition, due to the trade-off between the field factor and the pitch scaling, there exists an optimum pitch at 2.5 μm, which yields the highest emission of electrons. This work also confirms earlier work by the group on the emission characteristics and polarization dependence: at low pulse energy, the emission is in the multiphoton regime and has an $\sin^6(\theta)$ dependence on the polarization; at high pulse energy, the emission is in the strong-field tunneling regime and has an $\sin^2(\theta)$ dependence on the polarization.

Thesis Supervisor: Dr. Luis F. Velásquez-García

Title: Principal Research Scientist

## Acknowledgements

First, I would like to thank my research supervisor, Dr. Luis F. Velásquez-García, for giving me this opportunity to work on this project. He has given me extensive personal and professional guidance, and I have truly learned a great deal from him.

I am also heartily thankful to Dr. Michael Swanwick, who has provided me tremendous help during the project. He helped me develop an understanding of the project, and helped me get this project moving forward. He is a great mentor with patience and expertise.

I would also like to take this opportunity to thank Donnie Keathley and Yujia Yang for their help and advice to the experiments and simulations. My gratitude also goes to our group members: Philip Ponce de Leon, Dr. Eric V. Heubel, and Dr. Arash Akhavan Fomani, for their feedback and advice. Thanks also go to all MTL technicians and staffs for their help and valuable suggestions.

I would also like to show my gratitude to my best friends, Minshu Zhan and Fang Han, for their friendship, encouragement, and support.

At last, I would like to thank my family for their love and support. My parents have been extremely supportive throughout my study at MIT. They are always my inspiration and passion for moving forward.

# Contents

## List of Figures

## List of Tables

# Chapter 1. Introduction and Motivation

## 1.1 Introduction

Ultrafast (<1ps-long pulses) cathodes with spatially structured emission [1] are a new and expanding research area that could become the enabling technology for exciting applications such as free-electron lasers (FELs), tabletop coherent x-ray sources [2] and ultrafast imaging [3]. State-of-the-art ultrafast cathodes are flat surfaces that use highly reactive materials to lower the workfunction and increase the quantum efficiency of single-photon absorption for ultraviolet (UV) pulses. However, these devices have several disadvantages including (1) they need to be fabricated, stored and operated in ultra-high vacuum (UHV: $10^{-9}$-$10^{-12}$ Torr), and (2) producing high current density reduces the operational lifetimes due to the rapid degradation of the low workfunction materials.

Ultrafast photon-triggered field emission cathodes look promising to bypass these shortcomings. Strong-field electron tunneling occurs when the electric field of high-intensity optical pulses interacts with field enhancing structures, and electrons are tunneled from solids as a result [4]-[9]. Previous work on ultrafast photo-triggered field emission cathodes has focused either on **single** metal tips that are serially manufactured [10] or **single** Si tips [11]. At MIT's Microsystems Technology Laboratories (MTL), we use wafer-level semiconductor batch fabrication techniques to create photon-triggered field emission cathodes with massively multiplexed arrays of nano-sharp high-aspect-ratio silicon pillars with high uniformity (>100,000 tips, 1–64 million emitters.cm$^{-2}$). These devices have several advantages: (1) they can be fabricated and stored at atmospheric pressure, and operated in high vacuum level of $10^{-7}$ – $10^{-8}$ Torr (instead of UHV); (2) the nano-sharp tip (~12nm in diameter) of each high-aspect-ratio silicon pillar greatly enhances the incident electric field to cause emission of electrons from the tip surface; (3) the massive multiplexing (4.6-million tips.cm$^{-2}$) of the pillars increases the total current emission, and also structures the emission as a series of planar arrays of electron bunches, which are essential for coherent x-ray sources based on inverse Compton scattering [2].

This work is part of the project called compact ultrafast bright and intense x-ray sources (CUBIX). For tabletop coherent x-ray sources based on inverse Compton scattering to be possible, the photocathode needs to produce a uniform series of nanostructured charge sheets with sufficient charge over an extended period of time. As proposed in [2], photon-triggered field emission cathodes can produce an array of beamlets (bunches of electrons); these beamlets are then converted to a longitudinal density modulation by a transverse-to-longitudinal emittance exchange. Hence, photon-triggered field emission cathodes enable generating partially coherent x-ray properties by inverse Compton scattering. Photocathodes can increase the efficiency of x-ray production by several orders of magnitude, and the brilliance and flux of such compact x-ray sources are similar to major synchrotron facilities, but with orders of magnitude smaller footprint and power assumption. The overall proposed layout of CUBIX is outlined in Figure 1.

In this thesis, we explore the scaling down and multiplexing limits of photon-triggered field emission cathodes composed of arrays of nano-sharp high-aspect-ratio silicon pillars. We examine both the multi-photon regime and the strong-field tunneling regime of the emission process using near IR pulses at various pulse energies. In addition, we explore how the geometry of the array (e.g., pitch) and the morphology of the pillars (e.g., tip radius and height) affect the electron emission. We model the structure using 2D and 3D COMSOL Multiphysics, collect experimental data on actual devices, compare and explain the results from both simulations and experiments. This work provides a framework for optimizing the geometry and the morphology of pillars for future designers.

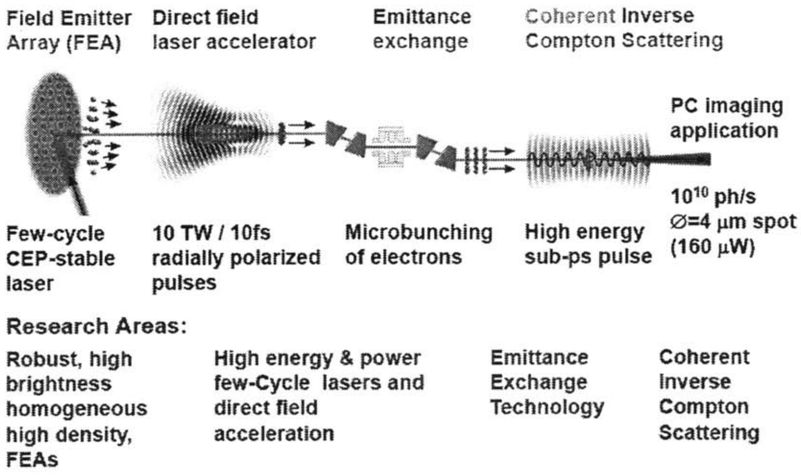

**Figure 1.** Schematic of the accelerator components and emittance-exchange beamline, proposed in [2].

## 1.2 Thesis Organization

The outline of the thesis is as follows:

Chapter 2 explains the theory of the photoemission and the field emission.

Chapter 3 briefly explains the device fabrication and process flow.

Chapter 4 explains the 3D and 2D models and their verifications in depth. We also provide evidence that supports the fact that the trend in the 3D models can be preserved in 2D models.

Chapter 5 explains the device characterization, including test set-up, test procedures and test samples.

Chapter 6 summarizes both the simulation result and the experimental result. We compare and intepret any similarities and discrepancies between both results.

Chapter 7 summarizes the work and possible ways to expand this work for future research.

# Chapter 2 Background and Theory

## 2.1 Theory of Field Emission

Electrons can be emitted from metal or semiconductor materials into vacuum through three distinctive processes: photoemission, thermionic emission, and field emission. In photoemission (as shown in Figure 2.a), electrons are emitted from the surface after being excited by photons with energy that is larger than the workfunction of the material, $\phi$, and the number of emitted electrons depends on the intensity of the beam. Photocathodes can produce ultra-short high-current pulses suitable for applications such as free-electron lasers [12], but they require UHV to operate due to their extreme sensitivity to contamination and humidity. In thermionic emission (as shown in Figure 2.b), electrons are emitted from the surface when the thermal energy of the electrons is larger than the workfunction of the material [13], so thermionic cathodes need to operate at high temperatures (over 1250K). However, operating at high temperatures could reduce the lifetime of the cathode if they operate in low vacuum and/or are exposed to reactive gases.

In field emission (as shown in Figure 2.c), electrons are emitted from the surface when a high electric, $F$, bends the vacuum level and reduces the barrier width. If the energy barrier is narrow enough, electrons quantum tunnel out of the surface. The emitted current density $J(F)$ is given by

$$J(F) = \int N(E_x)D(E_x, F)dE_x \qquad (1)$$

where $E_x$ is the kinetic energy of the electron along the emission direction $x$, $N(E_x)$ is the flux of carriers, and $D(E_x, F)$ is the transmission probability through the surface barrier. The flux $N(E_x)$ depends on the velocity of the electron in the $x$ direction, the density of states, and the Fermi function. The transmission probability, *D(E<sub></sub>*

$$D_{WKB}(E_x, F) = \exp\left(-2\sqrt{\frac{2m}{\hbar}}\int\sqrt{(\phi + E_f - E_x - qF)}dx\right) \qquad (2)$$

where $m$ is the electron's effective mass, where $\hbar$ is Planck's constant, $E_f$ is the Fermi level, $q$ is the electron's charge, and $x$ is the distance along the barrier width.

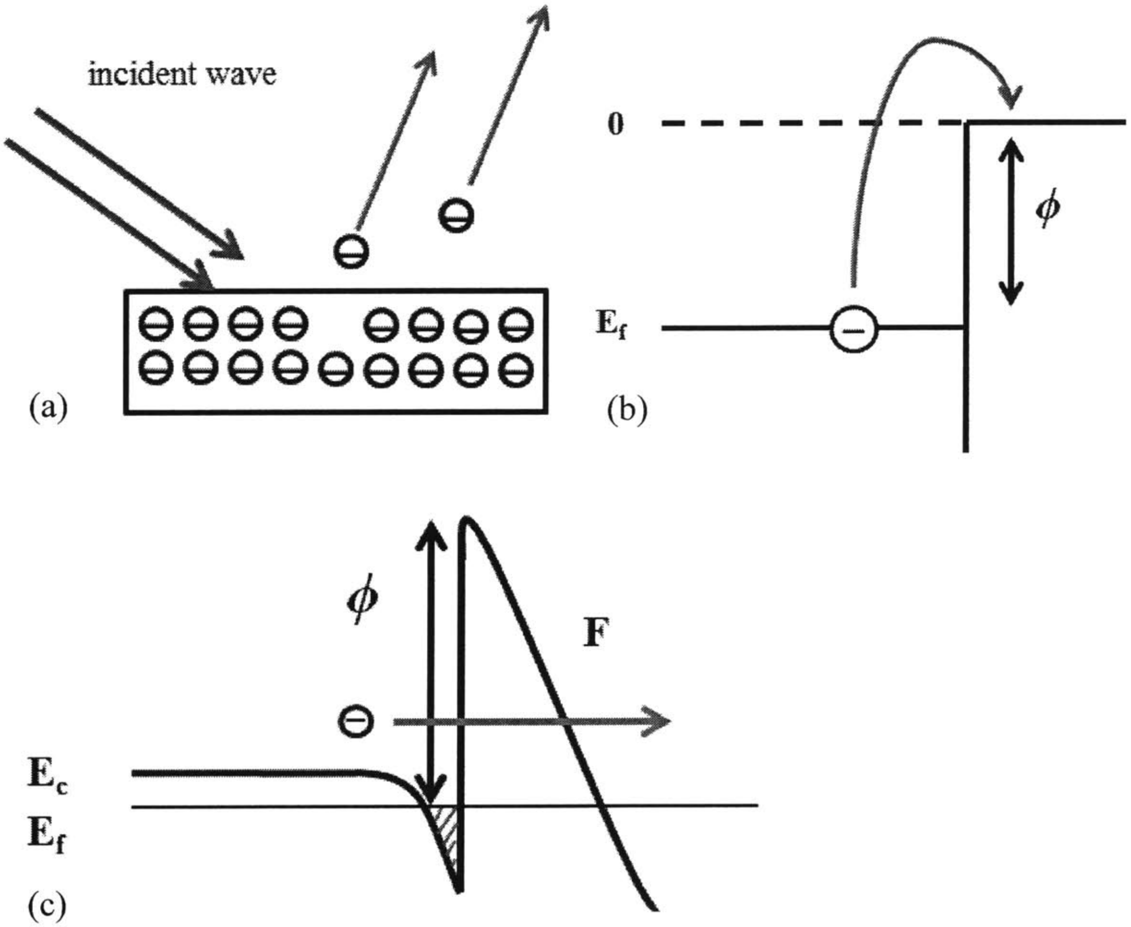

**Figure 2.** Three distinctive processes of electron emission: (a) photoelectric emission, (b) thermionic emission, and (c) field emission.

After simplifications and approximations, Equation 1 results in the well-known Fowler-Nordheim (FN) equation, which relates the field-emitted current to the electrostatic field at the surface [14]:

$$I = \alpha_{tip} \frac{A_{FN}}{\phi t^2(y)} F^2 exp \left[ \frac{-B_{FN} \phi^{2/3}}{F} v(y) \right] \qquad (3)$$

where $I$ is the current from the tip, $\alpha_{tip}$ is tip emitting area, $A_{FN}$ and $B_{FN}$ are constants, $t(y)$ and $v(y)$ are Nordheim elliptic functions. The FN equation states that field emission current has an exponential dependence with respect to the local electric field at the tip surface. The local electric field, $F$, is enhanced by the emitter tip from the electric field of the incident photons, and can be expressed as,

$$F = \beta_{eff} \cdot F_{photon} \qquad (4)$$

where $\beta_{eff}$ is the dimensionless field enhancement factor of the tip, and $E_{photon}$ is the electric field of the incident photons. In this project we extracted the dimensionless field factor from the simulations and investigated how it changes with respect to the inter-emitter spacing, the emitter height, and the emitter tip radius.

The electron emission of the photon-triggered field emission cathode can occur on either the multiphoton regime (as Figure 2.a) or strong-field tunneling regime (as Figure 2.c). In the multiphoton regime, electrons are excited by multiple photons to overcome the workfunction of the material; this mechanism takes place when the cathode is triggered with low incident energy (~ <0.3 μJ). The other regime, i.e., the strong-field tunneling, takes place when the cathode is triggered with high incident energy (~ > 1 μJ). A transition between the two regimes can be seen in the characteristic of the cathode, represented by a bending of the curve.

## 2.2 Objective and Technical Approach

In this work, we explore the scaling down and multiplexing limits of photon-triggered field emission cathodes composed of arrays of nano-sharp high-aspect-ratio single-crystal silicon pillars. We are interested in exploring and understanding the emission process by collecting the charge-energy characteristic of the device at various pulse energies, and investigating how the characteristic changes with the structure of the array. In addition, with the help of simulations, we explore how the geometry of the array (e.g., pitch) and the morphology of the pillars (e.g. tip radius and height) impact the electron emission. Then we compare and discuss both results, interpret and understand any similarities and discrepancies between the experimental result and the simulation result. We aim to extract a feedback loop to optimize the geometry and morphology of the device to achieve the highest emission and provide a framework for future designers.

## Chapter 3. Device Fabrication

All devices were fabricated by Dr. Michael Swanwick of MTL. Using a CMOS-compatible microfabrication process flow and ~5 Ω.cm n-type single-crystal wafers, we can fabricate very uniform tip arrays with under 1 nm standard deviation across a 150mm wafer and also from wafer to wafer [15]. First, an array of circular features is formed on the wafer using a 250 nm-thick chemical vapor deposited (LPCVD) silicon-rich silicon nitride film, projection optical lithography, and reactive ion etching (RIE). Then, a second array of circular features is created on top of the first array using a 500 nm-thick plasma enhanced chemical vapor deposited (PECVD) silicon dioxide film, projection optical lithography, and RIE; each oxide feature is concentric within 0.1 μm to the nitride feature right underneath. Next, the body of the pillars is etched using deep reactive ion etching (DRIE); the wafers are then cleaned and oxidized. The oxidation step thins the pillars and the nitride features act as a diffusion barrier to form the tips. The oxide and nitride films are removed using wet etchants, and highly uniform hexagonally packed arrays of single-crystal silicon pillars topped by an ultra-sharp tip are resulted. The process flow is summarized in Figure 3.

We fabricate silicon tip arrays with the pillar heights of 2 μm, 4 μm, and 8.5 μm, and pitches of 1.25 μm, 2.5 μm, 5 μm and 10 μm (1–64 million emitters.$cm^{-2}$). The summary of the tested devices is listed in Table 1 in Chapter 5. Figure 4 shows an SEM cross-section view of a fabricated array of high-aspect-ratio Si pillars with 1.25 μm pitch, 8.5 μm height and tip radius of ~6nm.

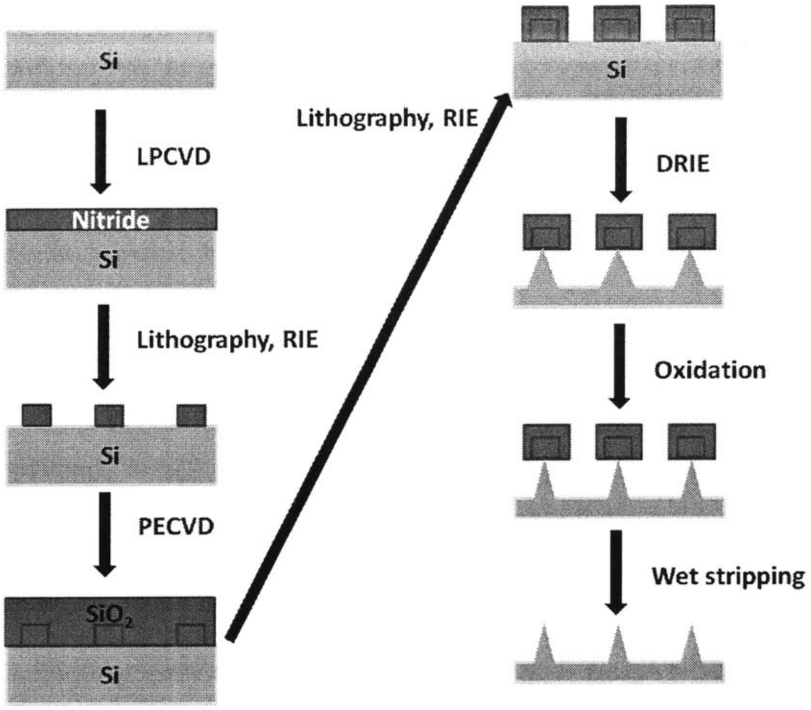

**Figure 3.** The process flow for fabricating arrays of single-crystal silicon pillars with an ultra-sharp tip.

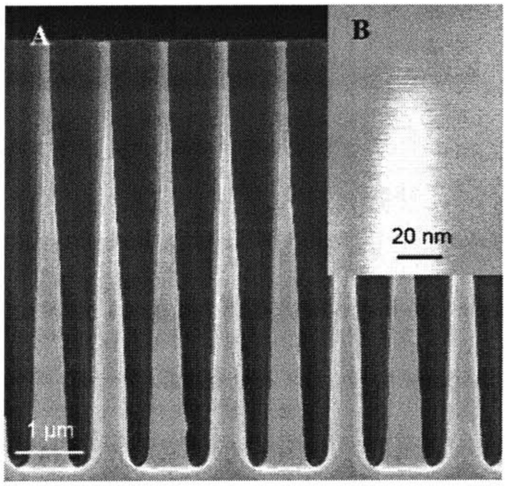

**Figure 4.** (a) SEM cross-section view of emitter array with 1.25 µm pitch and 8.5 µm height; (b) close-up of a single tip with an approximated radius of curvature of 6 nm.

# Chapter 4. Device Modeling

We used simulations to explore how the geometry and the morphology of the Si pillar enhance the electric field at the tip. It is not only cost-efficient and time-efficient, but also helps develop a feedback loop to design better devices. We used COMSOL Multiphysics to simulate the field enhancement of the structure near the tip. COMSOL takes advantage of a numerical technique called finite element method (FEM), which finds approximate solutions to boundary value problems for partial differential equations (PDEs). FEM divides a large domain into many small subdomains (called finite elements), solves each subdomains by minimizing an error function, and produces a stable solution for the large domain [16].

## 4.1 3D Simulation Model: Design & Verification

We needed to develop a 3D model to simulate an infinite 2D array of Si pillars. The geometry of the pillar should resemble the actual device seen in Chapter 3 – a cone structure with a hemispherical cap with a radius of 6nm. An efficient way to simulate an infinite 2D array is to simulate the unit cell with appropriate boundary conditions.

The complete 3D model is shown in Figure 5. It consists of a single tapered pillar 2.0 μm tall and 0.7 μm wide at the base with a 6 nm radius hemispherical cap. Perfectly Matched Layers (PMLs) are added on the top and bottom to absorb the excited and higher order modes. Floquet periodicity is applied on the four sides of the unit cell to simulate the infinite 2D array. The port boundary condition is applied on the interior boundary of the PML as the excitation port to radiate the 800nm incident wave at a glancing angle of 84° from normal (the same experimental setup described in [17]).

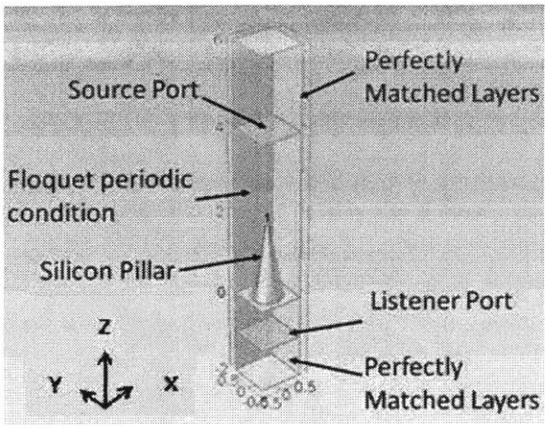

**Figure 5.** The 3D COMSOL model consists of a single pillar, PMLs on the top and bottom, Floquet periodicity on four sides and a source port with an incident 800nm wave at a glancing angle of 84°.

One important parameter we need to tune is the element size for meshing. A rule of thumb is that the maximum element size has to be less than one fifth of the wavelength [18]. In our case, since the wavelength is 800 nm, so the maximum element size has to be less than 160 nm in vacuum, and less than 46 nm in Si (due to Snell's law). Therefore, we picked the element sizes of 140 nm in vacuum and 40 nm in Si. Also, since the radius of the tip is very small (~6 nm), we need to mesh extra fine near the tip. Therefore, we defined a 50nm by 50nm cubic around the tip with the **maximum** element size of 5 nm. Figure 6 shows that the tip is well meshed with the element size of about 1.5 nm.

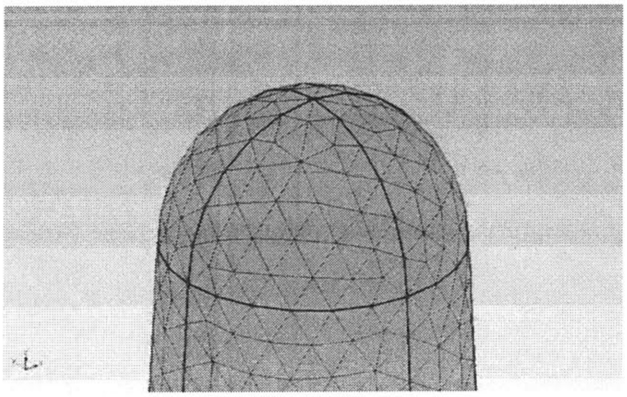

Figure 6. The tip is well meshed with the element size of about 1.5 nm.

After creating the model, we validated it by verifying the Fresnel equations between Si and vacuum before inserting the Si pillar. Fresnel equations describe the behavior of light when moving between media with different refractive indices. Equation 5 predicts the p-polarized reflectance between two media.

$$R_p = \left|\frac{n_1 \cos\theta_t - n_2 \cos\theta_i}{n_1 \cos\theta_t + n_2 \cos\theta_i}\right|^2 = \left|\frac{n_1\sqrt{1-\left(\frac{n_1}{n_2}\sin\theta_i\right)^2} - n_2\cos\theta_i}{n_1\sqrt{1-\left(\frac{n_1}{n_2}\sin\theta_i\right)^2} + n_2\cos\theta_i}\right|^2 \tag{5}$$

In our case, $n_1$ is the refractive index of vacuum and $n_2$ is the refractive index of Si, $\theta_i$ is the incident angle (84°), and $\theta_t$ is the refractive angle from Snell's law. Therefore, the analytical reflectance between Si and vacuum is 0.202. The simulated reflectance from our model is 0.194, and the error of 0.008 is within 4%. Therefore, it confirms that our model is correctly implemented.

As an example, we set the pitch to be 1μm and ran the simulation of the 3D model. A 2D slice contour plot (Figure 7) shows the simulated electric field from a 1 GV/m incident field on an emitter using frequency domain analysis. The maximum electric field at the tip is about 4.2 GV/m, i.e., the emitter tip has an enhancement factor of ~4.2. We further increased the pitch till 1.75 μm and plotted the corresponding field factors in Figure 8. Figure 8 shows ripples on the curve, which makes it hard to extract the relationship between the field factor and the pitch, so we would like to expand the model for pitches beyond 1.75 μm. However, at the pitch of 1.75 μm, the model has to solve about 6 million degrees of freedom, and takes more than 24 hours to converge. Running the model with 2 μm pitch required more computational memory beyond the capacity of MTL servers, so the solution never converges. As a result, we decide to switch to 2D model, which costs less memory and time, so we can expand the models for pitches beyond 2 μm.

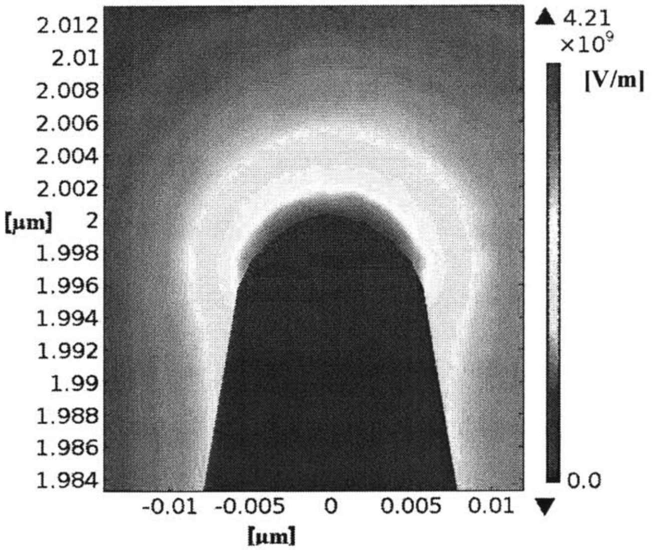

**Figure 7.** 2D slice contour plot from the 3D model with 1 μm pitch, 2 μm pillar height and a 1 GV/m incident field shows that the maximum electric field at the tip has a field enhancement factor of ~4.2.

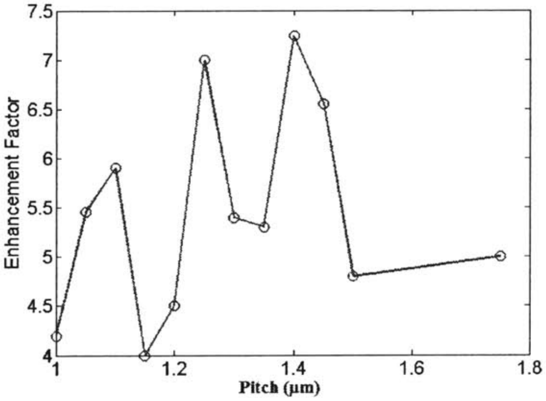

**Figure 8.** The plot of the enhancement factor vs. the pitch between 1μm and1.75 μm shows ripples.

### 4.2 2D Simulation Model: Design & Verification

The 2D model is very similar to 3D model by assuming symmetry in one axis (z-axis in our case). The complete 2D model is shown in Figure 9. However, due to losing one axis, the 2D model simulates infinite ridges on an infinite 1D array instead of the pillar in the 3D case.

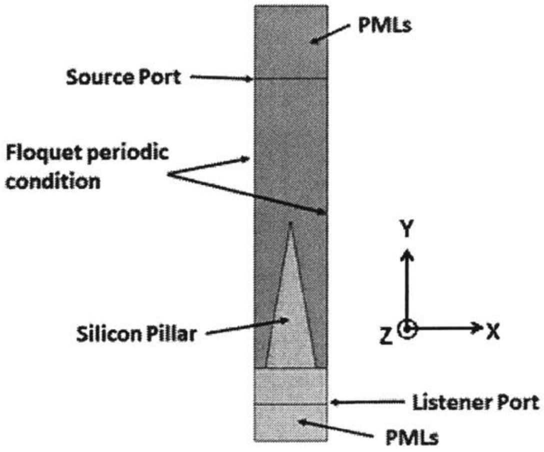

**Figure 9.** The 2D COMSOL model consists of a single pillar, PMLs on the top and bottom, floquet periodicity on two sides and a source port with an incident 800nm wave at a glancing angle of 84°.

Since 2D model is memory-efficient, we further decreased the maximum element sizes for meshing. For 2D models, we picked the maximum element sizes of 120 nm in vacuum, and 30 nm in Si.

Similarly, we validated the 2D model by verifying the Fresnel equation between Si and vacuum without the Si ridge. Recall that the analytical reflectance between Si and vacuum is 0.202. The simulated reflectance from 2D model is 0.196, and the error of 0.006 is within 3%. Therefore, it confirms that our 2D model is correctly implemented.

As an example, we set the pitch to be 1μm and ran the simulation of the 2D model. The 2D surface plot (Figure 10) shows the simulated electric field from a 1 GV/m incident field on an emitter using frequency domain analysis. The maximum electric field at the tip is about 1.7 GV/m, i.e., the emitter tip has an enhancement factor of ~1.7.

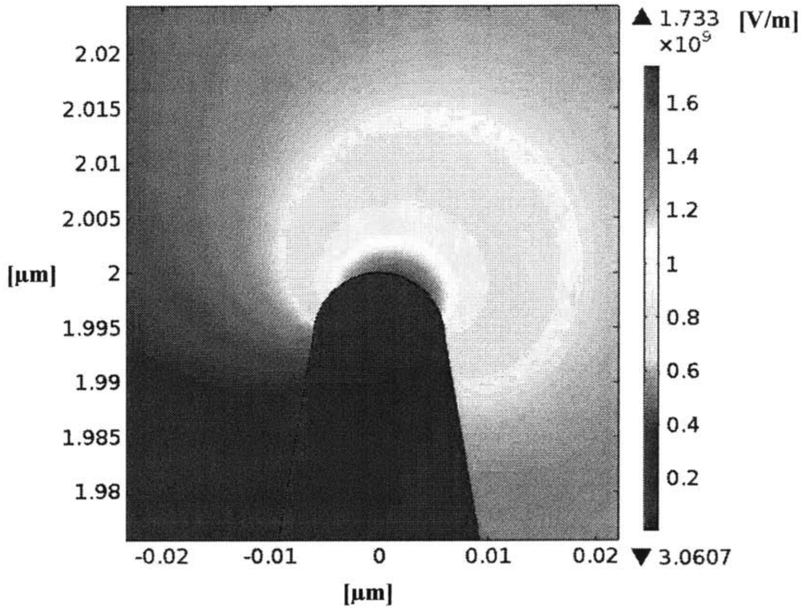

**Figure 10.** 2D surface plot from the 2D model with 1 μm pitch, 2 μm pillar height, and a 1 GV/m incident field, shows that the maximum electric field at the tip has a field enhancement factor of ~1.7.

Both Figure 8 and Figure 10 show the field enhancement for the same nominal structure, but the 3D model has a much larger enhancement factor than 2D model. This difference is due to the difference in the geometry of 3D model and 2D model, as 3D features more effectively concentrate the field lines compared to 2D features. The 3D model simulates a unit cell with one single **pillar**, while the 2D model simulates a unit cell with a single **ridge** (infinite in z-axis). Since we used TM mode, $E_z$ is zero for both models. With sin(84°)>>cos(84°), we can conclude that $E_{norm}$ can be represented well by $E_Y$ alone. It makes sense that $E_Y$ in the 2D model is visibly less than $E_Y$ in the 3D model because the wave interacts with the infinite ridge in 2D case, while the wave interacts with a hemispherical tip in 3D case. Hence, the field is less enhanced in the 2D case.

Figure 11 compares $E_X$ and $E_Y$ in both 2D and 3D models of similar structures (both simulate the structure with 1.5 μm pitch and 2 μm height). Even though both models show different field factors (~4.7 from the 3D model and ~1.8 from the 2D model), they show similar enhancement pattern near the tip in x-axis and y-axis. For example, both models result in two lobes in the x-direction, and one lobe in the y-direction. However, the field lines in the 3D models are more concentrated near the tip, while the field lines in the 2D model are more diverged. Because of the similar enhancement patter near the tip, we are confident that the trend in 3D model is preserved in 2D model, even though the numerical values are different.

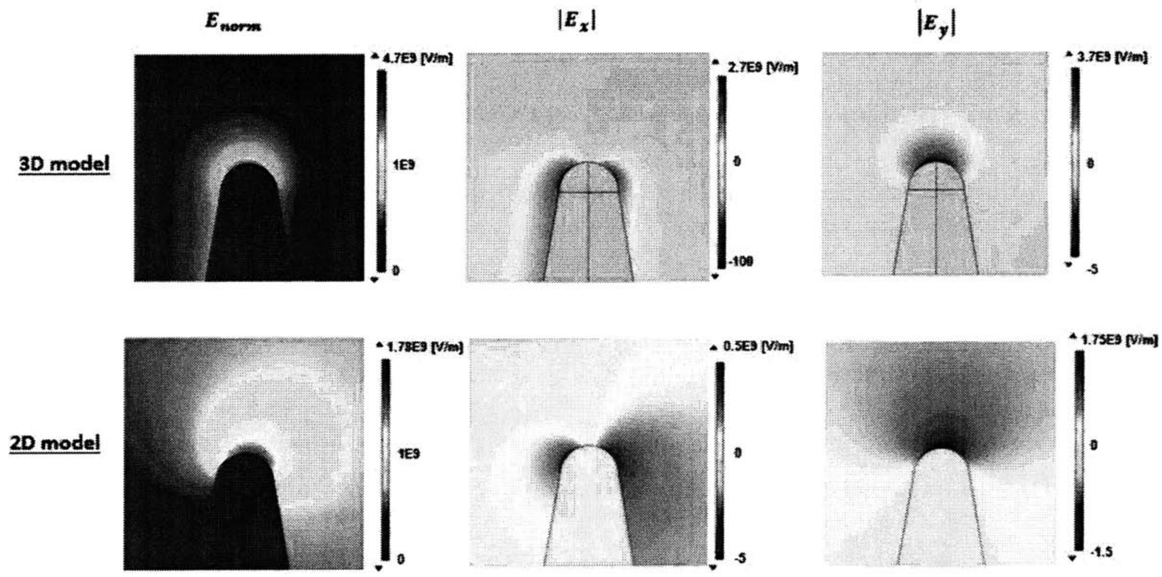

**Figure 11.** Both models simulate the structure with 1.5 μm pitch and 2 μm height with the same incident field of 1GV/m, and the enhancement patterns near the tip in the x-direction and y-direction are shown above. Given similar structures, both models show similar enhancement pattern.

More results from 2D simulations are discussed in Chapter 6.

## Chapter 5. Device Characterization

In this chapter, we discuss how the charge-energy characteristics of the devices were collected.

### 5.1 The photocathode vacuum system

The simplified schematic of the photocathode vacuum system is shown in Figure 12. The measurement takes place in a vacuum chamber, which was built by Dr. Michael Swanwick. The vacuum level inside the chamber is in the order of $10^{-7}$-$10^{-8}$ Torr. The chip is connected to ground through a picoammeter (Keithley 6485). The anode electrode, a 0.25" diameter plate, is placed 3 mm above the tips and is connected with a source-measuring unit (SMU: either Keithley 237or Keithley 248), which provides various voltage biases between 10V and 5000 V. The cathode was excited with 35 fs 800nm laser pulses at 3 kHz repetition rate from a regeneratively amplified titanium sapphire oscillator seed. The laser pulses hit the samples at an 84° grazing incidence, creating a 765 μm by 80 μm ellipse. The intensity of the incident wave is controlled by changing the waveplate angle through a LabView script and switching different filter lenses (0db, 10db and 20db). The data are collected using a LabView script. A close-up view of the actual chamber is shown in Figure 13.

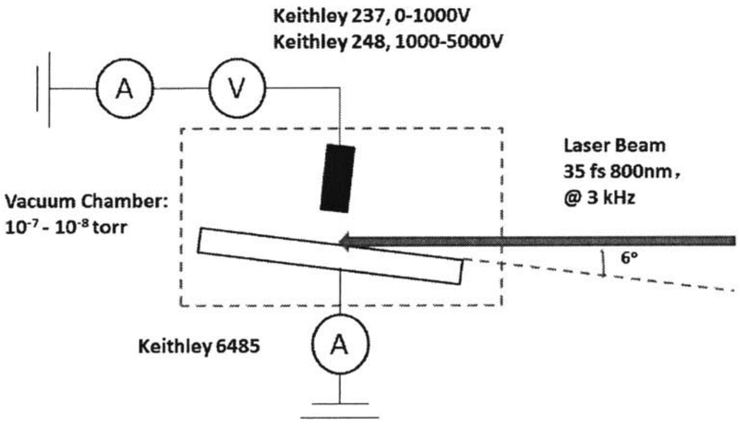

**Figure 12.** The simplified schematics of the photocathode vacuum system.

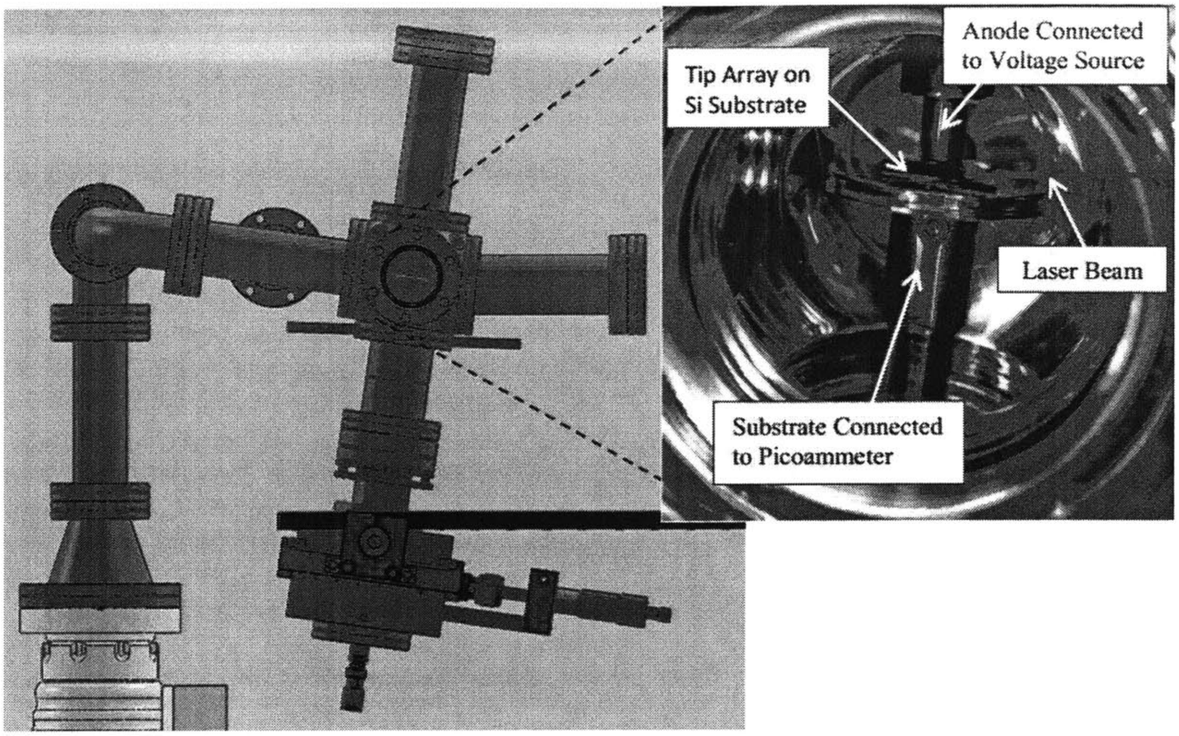

**Figure 13.** A close-up view of the actual chamber from [17].

### 5.2 Test procedure

Before testing, the chip is dipped in 2% HF acid to remove native oxide and then placed into the vacuum chamber. We start the turbo-molecular pump and diaphragm pump and wait till vacuum level falls to ~$10^{-8}$ Torr. The laser amplifier requires warming up for 1 hour before taking measurement. Then we align the laser with the center of the sample roughly. We also need to tune the polarization angle and the laser compression to maximize the current. The sample needs to sit in the chamber for at least 20 minutes with the voltage bias of 100V and the intensity of 1.4μJ (@6W, 10db) to stabilize current readings. We use Keithley 237 and Keithley 248 to sweep the anode bias between 10V and 5000V. At each voltage bias, we sweep the incident energy between ~$10^{-2}$ μJ and ~10 μJ, and record the current readings using a LabView script.

The data later are processed with MATLAB to obtain charge-energy characteristics. The result of experimental data is discussed in Chapter 6.

### 5.3 Table of Samples

We fabricate silicon emitter arrays with the pillar heights of 2 μm, 4 μm, and 8.5 μm, the pitches of 1.25 μm, 2.5 μm, 5 μm and 10 μm (1–64 million emitters.cm$^{-2}$) and constant taper, so there are totally 12 different kinds of devices. We tested at least one sample for each kind, and the samples we tested (recognized by the wafer number) are summarized in Table 1.

| **Index** | **Pitch (μm)** | **Height (μm)** | **Wafer Number** |
|---|---|---|---|
| **1** | 1.25 | 2 | W74 |
| **2** | 1.25 | 4 | W31, W73 |
| **3** | 1.25 | 8 | W32, W71 |
| **4** | 2.5 | 2 | W57 |
| **5** | 2.5 | 4 | W26, W60 |
| **6** | 2.5 | 8 | W28, W61 |
| **7** | 5 | 2 | W53 |
| **8** | 5 | 4 | W52 |
| **9** | 5 | 8 | W51 |
| **10** | 10 | 2 | W65 |
| **11** | 10 | 4 | W64 |
| **12** | 10 | 8 | W39, W63 |

**Table 1.** The summary of the tested samples.

# Chapter 6. Results and Discussion

In this chapter, we discuss and compare the results from both simulations and experimental data, and explain any discrepancies.

## 6.1 Simulation Results

According to the Fowler-Nordheim equation (i.e. Equation 3), the field emission of electrons depends exponentially on the field enhancement. If we can increase the field enhancement at the tip, we will achieve the same emission by using pulses orders of magnitude less intense. We used 2D models to explore how the geometry and the morphology of Si pillar enhance the electric field at the tip. There are several parameters that we are interested in studying. First, we want to know how the radius of hemispherical tip affects the field enhancement. The field enhancement factor is proportional to $1/r^n$ or $r^{-n}$, where $r$ is the tip radius, and $n > 0$. If our simulations verify this relationship, we are confident about the 2D models. Second, we are interested in how the pitch, i.e., the distance between each pillar, affects the field enhancement. Third, we want to explore how the pillar height affects the field enhancement. Since taller pillars require longer etching step and are hence more costly and harder to make, it is preferred to fabricate shorter pillars.

We simulated arrays with pitches between 1 μm and 100 μm and the fixed height of 2 μm for tip radii of 6 nm, 12 nm, and 24 nm, and the result is shown in Figure 14.a. We also extracted a numerical model which relates the field factor at the fixed pitch of 100 μm to the tip radius as shown in Figure 14.b. The model has a negative power dependence factor (i.e. −0.278) on the tip radius, which agrees with the expected trend. It means that the field factor is a strictly decreasing function of the tip radius. In addition, 2D models lose the z-axis (as shown in Figure 9), so it is insensitive to the change of the tip radius in the z-axis. Therefore, we expect to observe a stronger power dependence factor in the 3D case.

Figure 14.a also shows that the field enhancement is strictly increasing with respect to the pitch. In the low-pitch range, the field enhancement increases rapidly due to the decreasing tip-to-tip shadowing as the pitch increases [17]. In the high-pitch range, the field enhancement saturates, because when the pitch is large enough (approaching to infinity), pillars are far apart and it is equivalent to simulate a single pillar on an infinite 2D array, whose field enhancement should be constant.

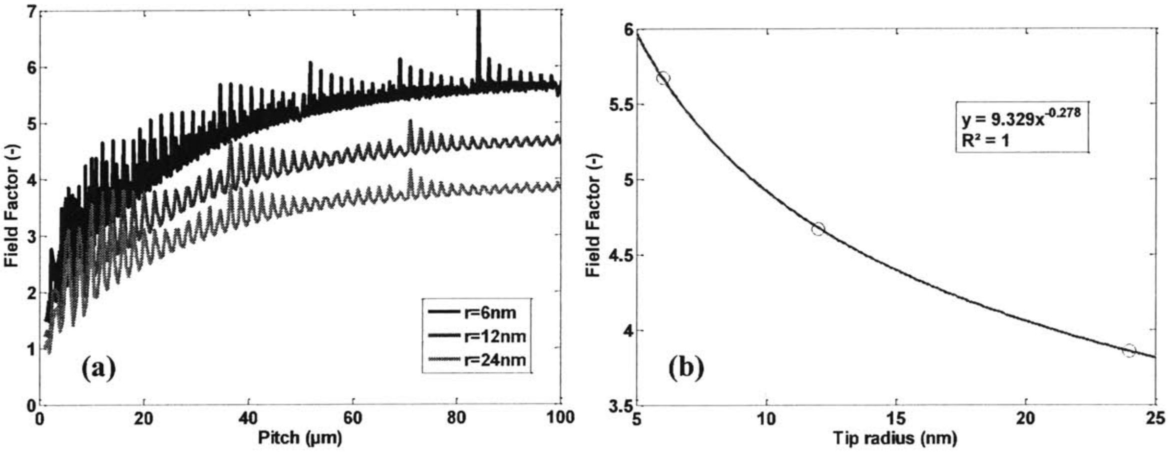

**Figure 14.** (a) Plot of the field factor vs. the pitch for various tip radii of 6 nm, 12nm, and 24 nm, with pitches between 1 μm and 100 μm, and the fixed height of 2 μm, (b) a power fit was extracted for the relationship between the field factor at the fixed pitch of 100 μm and the tip radius.

The curves in Figure 14.a have ripples, and these ripples seem to repeat periodically. To further explore these ripples, we run finer sweeps of the pitch range with the step size of 10nm, and the result shows that the period of these ripples is about 400 nm, which is half of the wavelength of incident wave (800 nm). In order to confirm this relationship between the ripple period and the wavelength, we set the wavelength at 800 nm, 900 nm, 1000 nm and 2000 nm, and the result is shown in Figure 15. The ripples are indeed periodic and their periods are summarized in Table 2. The period is a little over half of the wavelength consistently, but no particular relationship between the amplitude of the ripples and the wavelength was found.

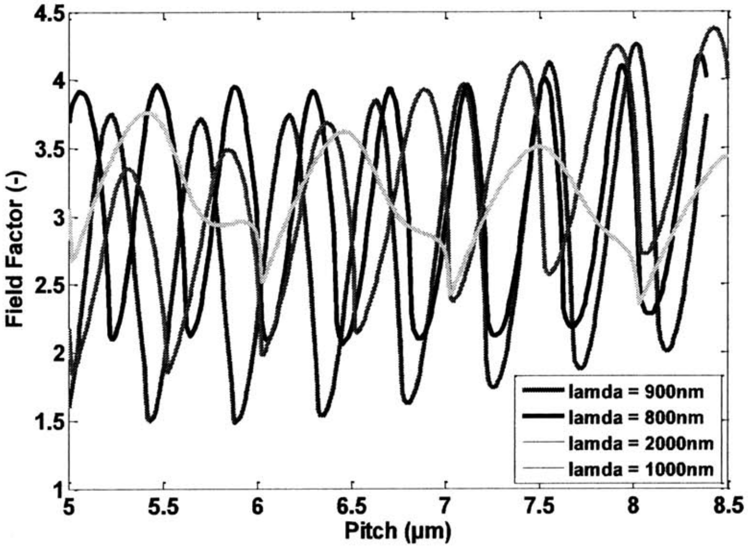

**Figure 15.** Field factor vs. pitch between 5 μm and 8.5 μm with the step size of 10 nm for various wavelengths shows that the ripples are periodic and the period is proportional to the wavelength of the incident wave.

| Wavelength λ (nm) | Peak to Peak Period (nm) | Ratio |
|---|---|---|
| 800 | 411 | 0.514 |
| 900 | 465 | 0.517 |
| 1000 | 518 | 0.518 |
| 2000 | 1040 | 0.52 |

**Table 2.** Summary of the incident wavelength and the ripple period. The period of the ripples is about half of the wavelength in all cases.

The occurrence of these ripples can be explained by Bragg diffraction. When electromagnetic radiation with wavelength comparable to atomic spacing is incident upon a crystalline sample, the waves are scattered in a specular fashion by the atoms in the system. They can undergo constructive or destructive interference. The constructive interference results in very strong intensities known as Bragg peaks, which follow the Bragg's Law [19].

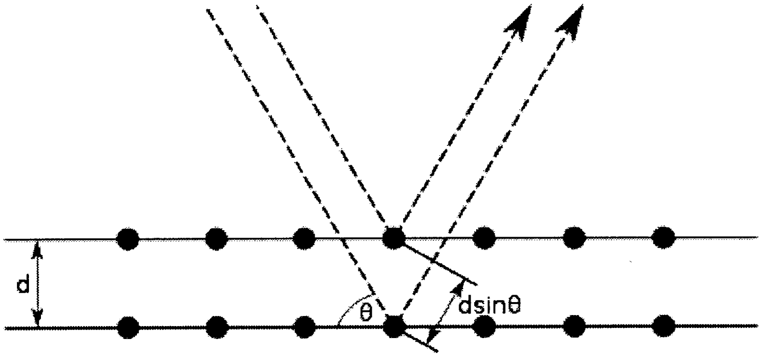

**Figure 16.** The mechanism of the Bragg diffraction at the atomic level. The incident waves are scattered off by atoms (black dots) and the Bragg peaks occur when the scattered waves are in constructive interference [20].

Figure 16 illustrates the mechanism of the Bragg diffraction at the atomic level. Two incident waves with identical wavelength, $\lambda$, and identical incident angle, $\theta$, approach a lattice of atoms with identical spacing, $d$. The waves are scattered off by two adjacent atoms within the lattice. The lower beam traverses an extra length of $2d\sin\theta$. Constructive interference occurs when the two scattered beams are in phase, i.e. when this extra length is equal to an integer multiple of the wavelength of the radiation.

In our case, we treat Si pillars as the black dots in Figure 16. Then the spacing, $d$, becomes the pitch between the pillars. Therefore, we can derive Equation 6 from the Bragg's Law, where $p$ is the period between peaks in the field enhancement function, $\lambda$ is the wavelength, $\theta$ is the incident angle, and $n$ equal to 1 (the minimal cycle).

$$p = \frac{n\lambda}{2\sin\theta} = \frac{\lambda}{2\sin\theta} \qquad (6)$$

Since the incident angle is 84°, $\sin\theta \approx 1$, and by Equation 6, $p \approx \lambda/2$. So the period is about half of the wavelength, which agrees with the simulation result. However, if we substitute the precise incident angle (84°) into Equation 6, the ratio of period to wavelength is 0.503, which is smaller than the ratios listed in Table 2. We propose two possible explanations for the discrepancy. First, simulations usually have some numerical artifacts [21]. Therefore, this discrepancy is possibly just a byproduct of numerical artifacts. Second, we simplify our problem by treating the Si pillars as atoms (or black dots), so we ignore the impact of the geometry of the pillar, which can affect the diffraction pattern.

We are also interested in how the height affects the field enhancement. As mentioned above, it is harder and more costly to make taller pillars, so shorter pillars are preferred. We vary the height of the pillar from 0.2 μm to 2 μm in the simulations and the result is shown in Figure 17.

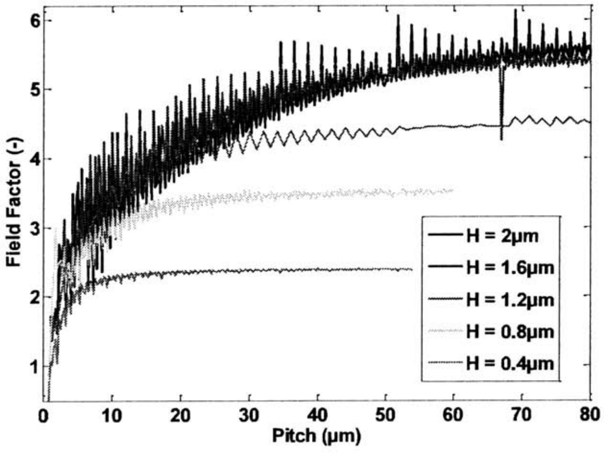

**Figure 17.** Field factor vs. pitch for various heights between 0.4 μm and 2 μm. The simulations show that the field enhancement is a strictly increasing function of the pillar height with a diminishing return. For example, the field factor of 2.0 μm is only slightly greater than the field factor of 1.6 μm.

For all the heights we simulate, we observe that the similar trend in Figure 14, i.e. the field enhancement increases rapidly in the low-pitch region and saturates in the high-pitch region. Also, it is clear that the enhancement factor is a strictly increasing function of the height of pillar, but this relationship is not linear. For example, the enhancement of the 2.0 µm tall pillar is only slightly greater than that of the 1.6 µm tall pillar. Therefore, the effect of the height on the field enhancement is diminishing. At some point, even if we continue increasing the height, the field enhancement should be about the same.

Another interesting finding of Figure 17 is that the ripple amplitude is a strictly increasing function of the pillar height. This can be explained by the mechanism shown in Figure 18. Imagine that the black dots on Figure 16 have some depth, i.e. the pillar height. When the surface is smooth or the pillar height is small, the waves are reflected by both the surface and the tips, so the difference in paths is not in phase, which results in mild ripples. When the height is large, some incident waves are trapped between two pillars and only the interference of the beams reflected by the tips is observed, so the difference in paths is common to all reflected beams and strong Bragg's diffraction occurs.

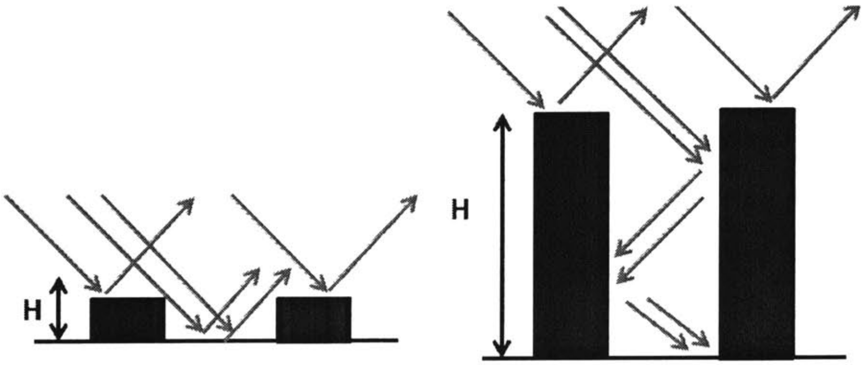

**Figure 18.** When the depth, i.e. pillar height, increases, some incident beams are trapped between two pillars, and only the interference of the beams reflected by the tips is observed, so the paths have the exact difference of length and the pure Bragg's diffraction occurs.

We are interested in extracting the relationship between the field factor and the pitch when the height is constant. We fit several numerical models (such as the logarithmic fit and the exponential fit) using the least square regression, and chose the exponential fit to describe the relationship between the field factor and the pitch for constant heights. The plot of the field factor predicted by the model of exponential fit for various heights between 0.4 μm and 2 μm is shown in Figure 19. There are two reasons for choosing the exponential fit: first, the exponential fit gives the largest R squared; second, the exponential model predicts that the field factor saturates at the high pitch, which agrees with the diminishing return of the pitch observed in Figure 17. We also observe that the exponential dependence factor (i.e. the coefficients in front of the pitch, $x$) becomes less negative as the pillar height increases. It means that, as the pillar height increases, a larger pitch is needed to achieve the same level of saturation. A numerical analysis on the level of saturation is discussed later in Figure 22.

We are also interested in finding how the saturated field factor, i.e. the field factor when the pitch is very large, is related to the height. We extract the saturated field factor from Figure 19, and then we fit several numerical models including the logarithmic fit, the square root fit, and the exponential fit, using the least square regression.

We decided to choose the exponential fit (as shown in Figure 20) to represent the relationship between the saturated field factor and the height because (1) the exponential fit has the largest R squared value, (2) the model predicts that the field factor will saturate around 9.4, which agrees with the diminishing return of the increasing height and pitch.

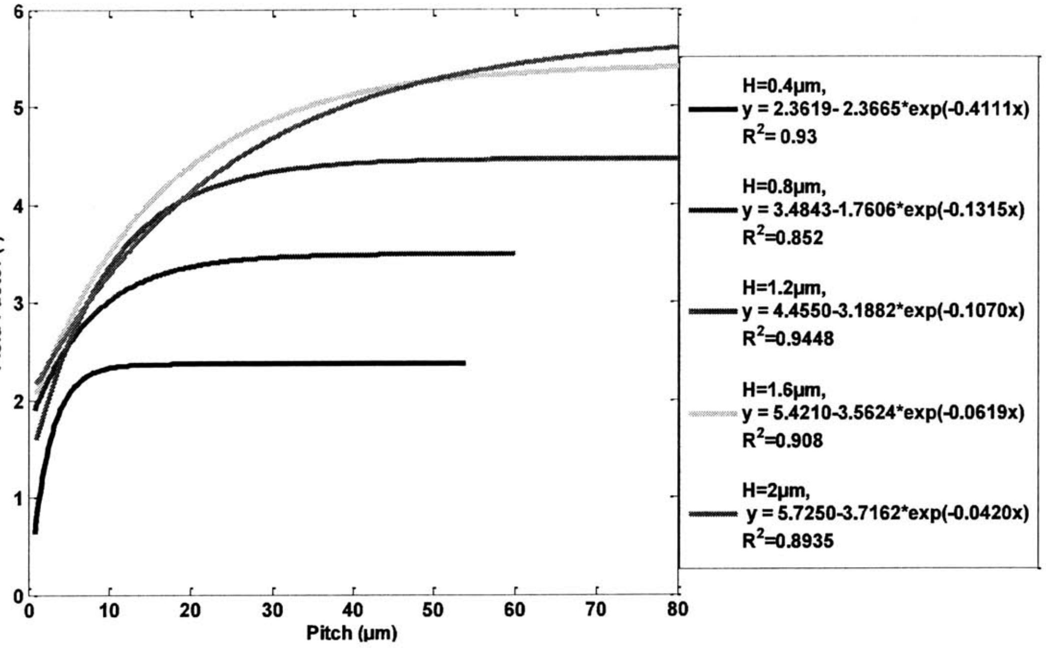

**Figure 19.** The plot of the field factor predicted by the model of exponential fit vs. the pitch for various heights between 0.4 µm and 2 µm. The equations and $R^2$ values are listed in the legend for all the heights, where *y* is the field factor and *x* is the pitch.

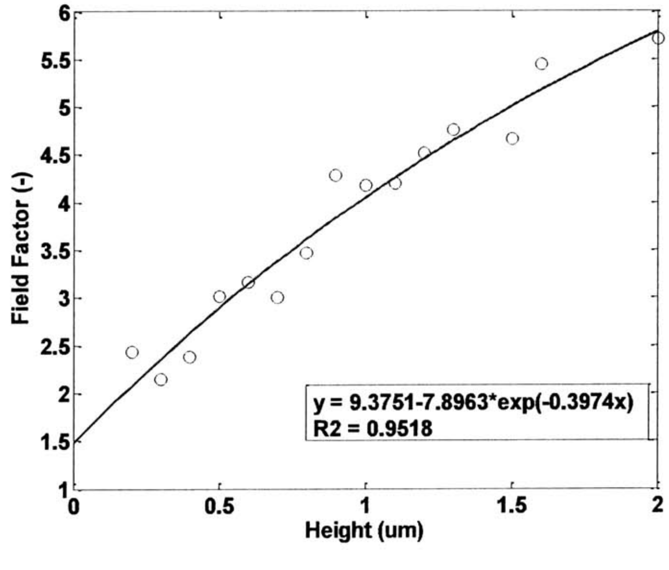

**Figure 20.** The plot of the saturated field factor predicted by the model of exponential fit vs. the height.

We would like to expand the simulation for structures with heights above 2 μm since we fabricated devices with heights of 4 μm and 8.5 μm. However, as shown in Figure 21, the field factor doesn't saturate as Figure 17 for pillar heights above 2 μm; the curves bend down instead, which is unexpected. One possible explanation is that the numerical artifacts for models with pillars height > 2 μm are too large. From first principles, we expect increasing height to help the field factor, as the influence of the flat surface would be less (as shown in Figure 18).

So far, we have seen several trends: (1) the field factor has a negative power dependence factor on the tip radius (i.e. the field factor is a strictly decreasing function of the tip radius), (2) the electric field is enhanced rapidly in the low-pitch region and saturates in the high-pitch region, and the relationship between the field factor and the pitch at the fixed height can be described by an exponential decay as shown in Figure 19, (3) the saturated field factor is a strictly increasing function of the height with a diminishing return and this relationship can be described by the model of exponential fit as shown in Figure 20.

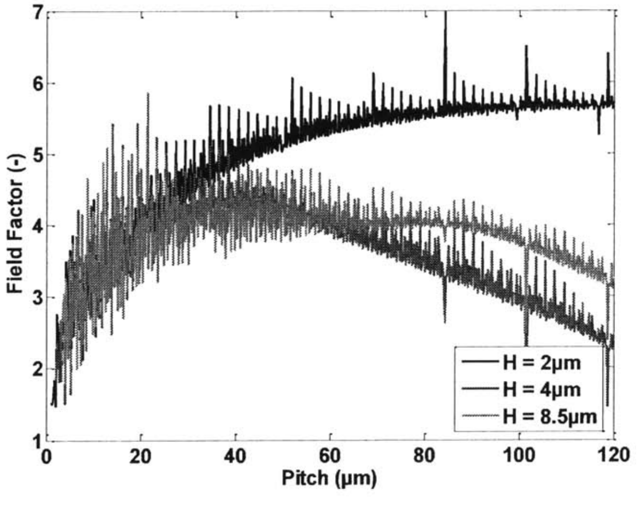

**Figure 21.** The plot of the field factor vs. the pitch at the heights of 2 μm, 4 μm and 8.5 μm. For pillar heights above 2 μm, the field enhancement doesn't saturate as in Figure 17; instead it bends down.

In practice, the designers may face more specific problems. For instance, if we want to fix the pillar height to be 2 μm, how could we choose the pitch to maximize current emission? On the one hand, we want the pitch as small as possible so that we can increase the emission of electrons by increasing the number of emitters. On the other hand, we want to increase the pitch so that it can reach its best field enhancement. Clearly, the designer faces a trade-off here, so we are particularly interested in finding the ideal pitch to height ratio which allows *almost* the best field enhancement while being packed as close as possible. In other words, what is the minimum pitch to height ratio that allows the enhancement factor reaches 90%, 95%, or 99% of its best or saturated value? We use the smooth curves and the saturated field factor in Figure 19 to extract the combination of height and pitch, which reaches 90%, 95% and 99% of the saturated value, and plot these points in Figure 22.

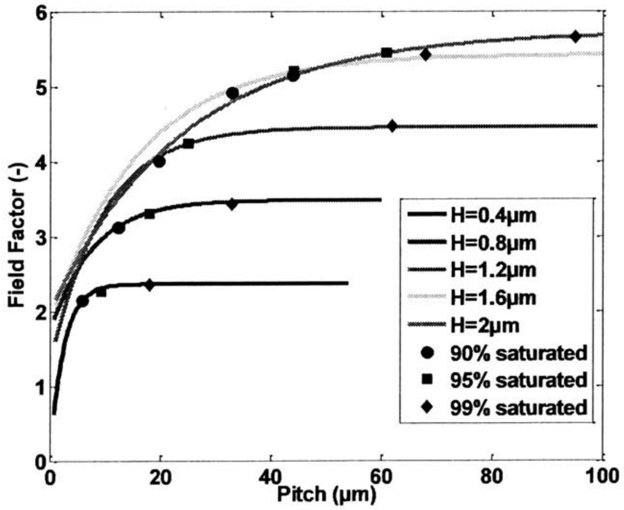

**Figure 22.** Plot of the field factor vs. the pitch for various heights. For each height, we extract the combination of height and pitch which reaches 90%, 95%, and 99% of its saturated value.

The pitch to the height ratios that reach 90%, 95% and 99% of the saturated value are summarized in Table 3. We also add the average of the ratios and the standard deviation as percentage of the average. The ratios that reach 99% of the saturated have the smallest standard deviation percentage, so it is more consistent. If we want to achieve 99% of the saturated field factor, according to Table 3, we need to make the pitch about 46 times the emitter height. These ratios can help designers determine the appropriate combination of pitch and height for different applications.

| **Height (µm)** | **99% Ratio** | **95% Ratio** | **90% Ratio** |
|---|---|---|---|
| 0.4 | 45 | 23.2 | 14.25 |
| 0.8 | 41.25 | 22.625 | 15.375 |
| 1.2 | 51.7 | 20.83 | 16.5 |
| 1.6 | 42.5 | 27.69 | 20.625 |
| 2.0 | 47.5 | 30.5 | 22 |
| **Average** | 45.58 | 24.97 | 17.75 |
| **Standard Deviation as % of the average** | 9.13% | 16% | 19% |

**Table 3.** The summary of the pitch to height ratios that reach 99%, 95%, and 90% of the saturated values.

## 6.2 Experimental Results

We test the devices listed in Table 1 following the procedure described in Section 5.3 and process the data using MATLAB scripts. From the last section, we observe that the field enhancement is a strictly increasing function of the height, which can be modeled by the equation in Figure 20. We are interested in whether it holds true for the actual devices. At the fixed pitches of 1.25 μm, 2.5 μm, 5 μm, and 10 μm, we compare the charge-energy characteristics (the incident energy as x-axis and total emitted charge as y-axis) for various heights of 2 μm, 4 μm, and 8.5 μm at the anode bias of 1000V.

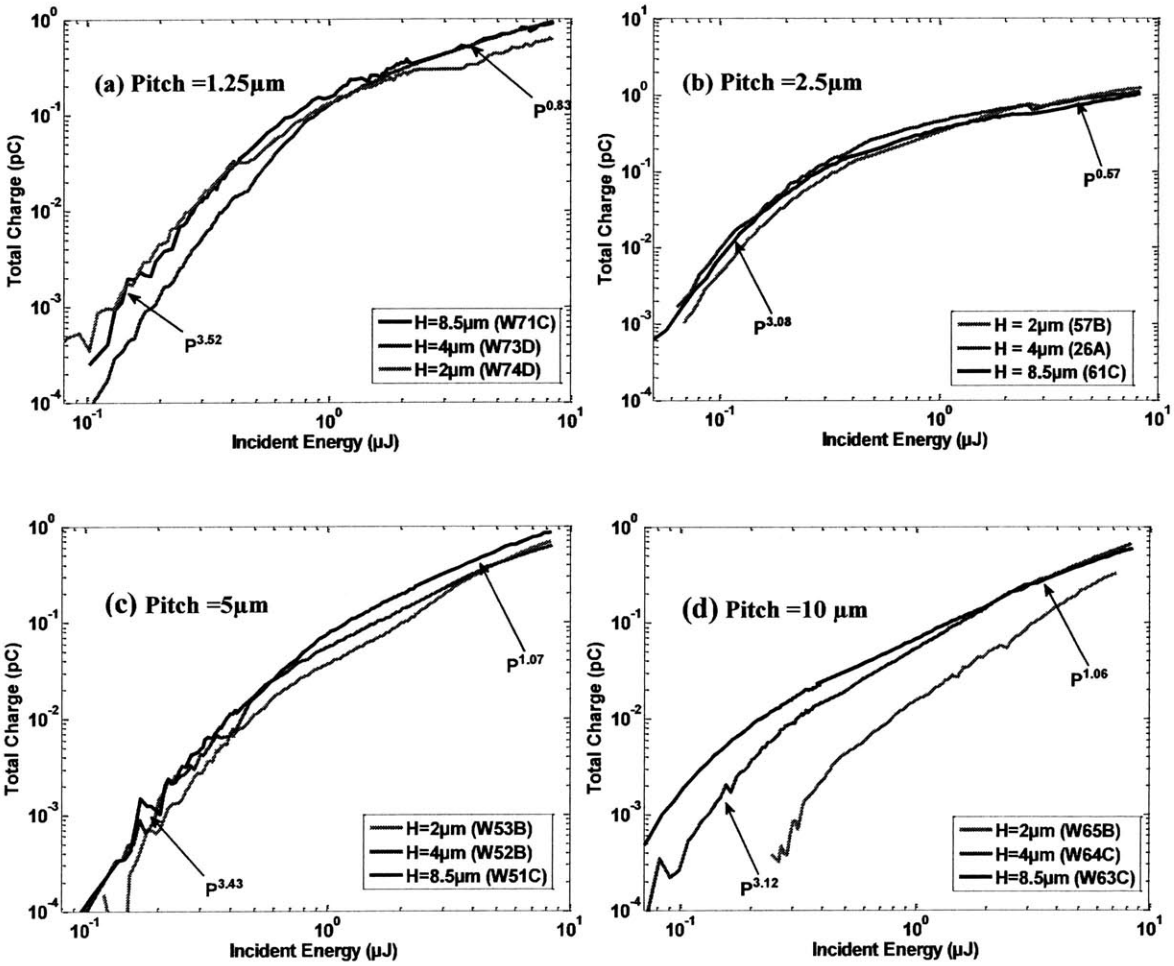

**Figure 23.** Total emitted charge vs. incident energy for various heights of 2 μm, 4 μm, and 8.5 μm at the fixed pitches of (a) 1.25 μm, (b) 2.5 μm, (c) 5 μm and (d) 10 μm at the anode bias of 1000V. In each plot, we also label their power dependence slopes in both low and high intensities where *P* means the incident energy.

From Figure 23, we observe that the emission has two processes: multi-photon process and tunneling process. At low intensities, since the electric field at the tip is not strong enough to bend the potential barrier, we expect the electron to absorb **three** photons simultaneously in order to escape from the tip surface, since the electron affinity of Si is 4.05 eV, and the photon energy with the wavelength of 800 nm is 1.55 eV. As shown in Figure 23, the power dependence slopes for all pitches are over 3 at low intensities (<0.3 μJ), so the experimental result agrees with the three-photon absorption process.

As we increase the intensity of the laser pulses, the electric field at the tip increases and the electrons tunnel into the continuum faster than they can oscillate back into the tips [22], [23]. This regime is commonly referred to as the strong-field or tunneling regime and it follows a time-averaged Fowler-Nordheim model [24]. For high pulse energy, the strong field emission model in [25] predicts that the slope at the highest current yield is ~1.2 at the fixed bias of 1000V without the consideration of space charge. Figure 23 (c) and (d) both have slopes (1.07 and 1.06) close to 1.2. However, Figure 23 (a) and (b) have slopes less than 1. This can be explained by the development of a space-charge induced virtual cathode [25] at lower pitches (1.25 μm and 2.5 μm). As electrons form a current sheet above the emitter, this virtual cathode suppresses the electron emission [26]. The strong field emission model in [25] with the consideration of space-charge limitation predicts a slope of 0.51 at the highest current yield with the bias of 1000V. This value agrees with the slopes of Figure 23 (a) and (b). The effect of the virtual cathode is worse at the lower pitches (1.25 μm and 2.5 μm), which may be due to the closer packing of pillars at the lower pitches.

Now we can explore how the height of pillars affects the emission of the actual devices. In Figure 23 (d), the charge emission is strictly increasing with respect to the pillar height, which agrees with the simulation result. In Figure 23 (a), (b) and (c), the charge emission is almost the same for different heights. Therefore, as the pitch decreases, the effect of the pillar height is diminishing. This is consistent with the simulation result. In Figure 17, the field factors for various heights overlap at low pitch (<10 µm), and spread out at high pitch, so the effect of the pillar height is not significant at smaller pitch compared to larger pitch. Therefore, we observe that the pillar height has a larger impact on the charge emission for the pitch of 10 µm.

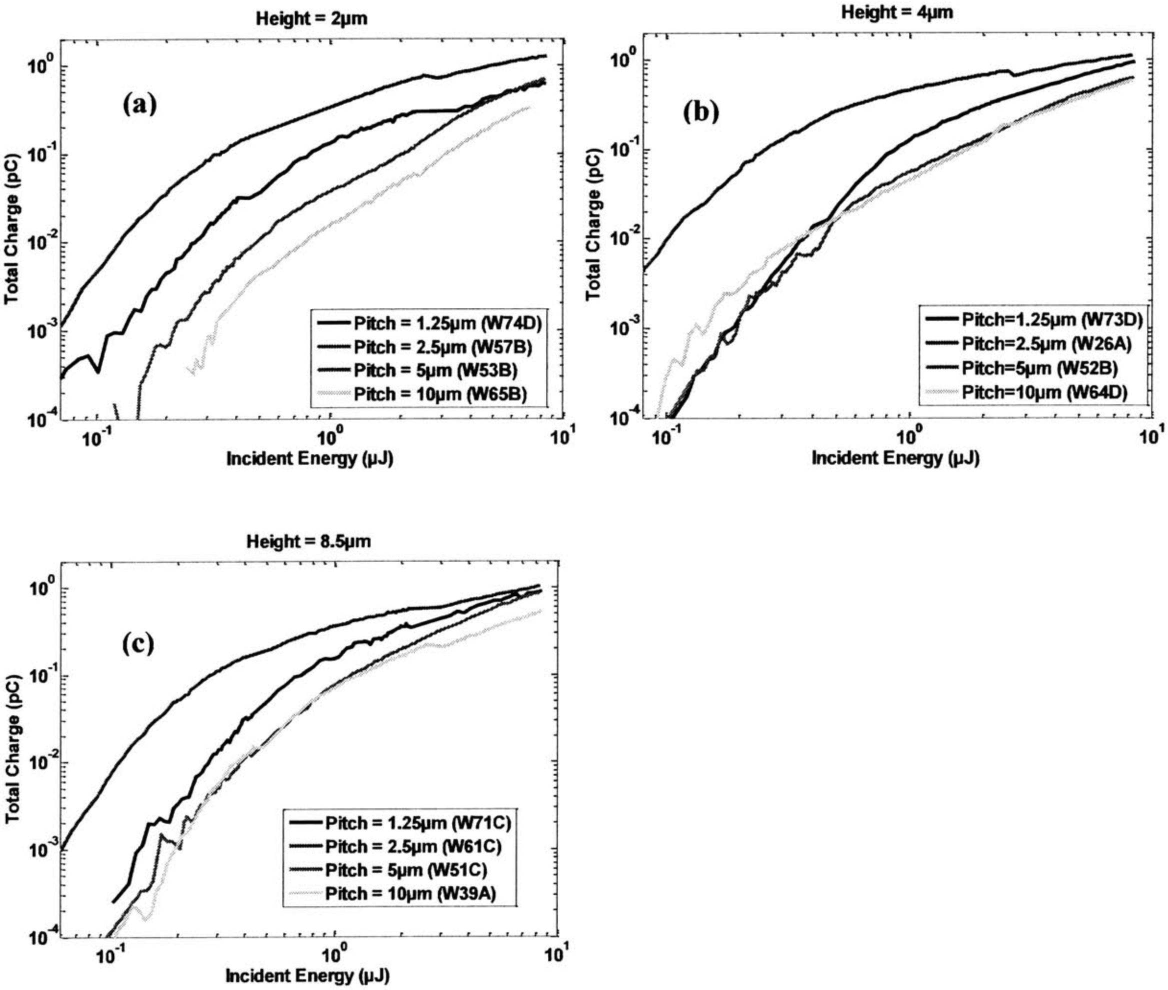

**Figure 24.** Charge-energy characteristics at pitches of 1.25 µm, 2.5 µm, 5 µm and 10 µm given pillar heights of (a) 2µm, (b) 4 µm, and (c) 8.5µm at the anode bias of 1000V.

We can also explore how the pitch affects the emission of electrons. In Figure 24, we plot the charge-energy characteristics at various pitches of 1.25 μm, 2.5 μm, 5 μm and 10 μm given pillar heights of 2μm, 4 μm, and 8.5 μm at the anode bias of 1000V. In the last section, the simulation result shows the field factor is a strictly increasing function of the pitch, which can be modeled by the equation in Figure 19. The total emission increases as the pitch increases if we compare the total emissions of devices with pitches equal to 1.25 μm, 5 μm and 10 μm. However, the emission is not only related to the field enhancement, but also related to the number of emitters on the array. This is the trade-off between the field enhancement and the pitch scaling mentioned in the last section: as we decrease the pitch, the decrease of the field enhancement can be compensated by the increase of number of tips on the array. From the experimental results, we observe that the pitch of 2.5 μm produces the highest total charge emission, but it doesn't necessarily means that 2.5 μm is the optimum pitch since we varied the height and pitch using a few discretized values of the ranges.

Another interesting observation from Figure 24 is that the charge-energy curves are converging at the high intensities. However, the convergence seems to take place for intensities beyond 10 μJ, which is close to the threshold energy for damage of the device [17].

To verify whether these trends hold true for another voltage bias, we also plot the charge-energy characteristics at a fixed bias of 100V for pillar heights of 2 μm, 4 μm and 8.5 μm. Figure 25 (a), (b), and (c) show very similar charge-energy characteristics as Figure 24 (a), (b) and (c), so we are confident that these trends hold true for other biases as well.

We are also interested in exploring how the emission per tip will vary with the pitch. To obtain the plot of the emission per tip, we need to calculate how many emitters the laser spot (a 765 μm by 80 μm ellipse) bathes for each pitch. We know that the number of emitters for the array of

5um pitch is ~2220 [17], and we also know that the number of emitters is proportional to $1/(1.15 \cdot pitch^2)$, where the factor of 1.15 reflects the hexagonal packing of the array. Therefore, we can calculate numbers of emitters for each pitch. Figure 26 shows that the larger pitch gives a better emission per emitter, especially at high intensities (>~3µJ). This is due to the better field enhancement at the tip at larger pitch, which agrees with the simulation result.

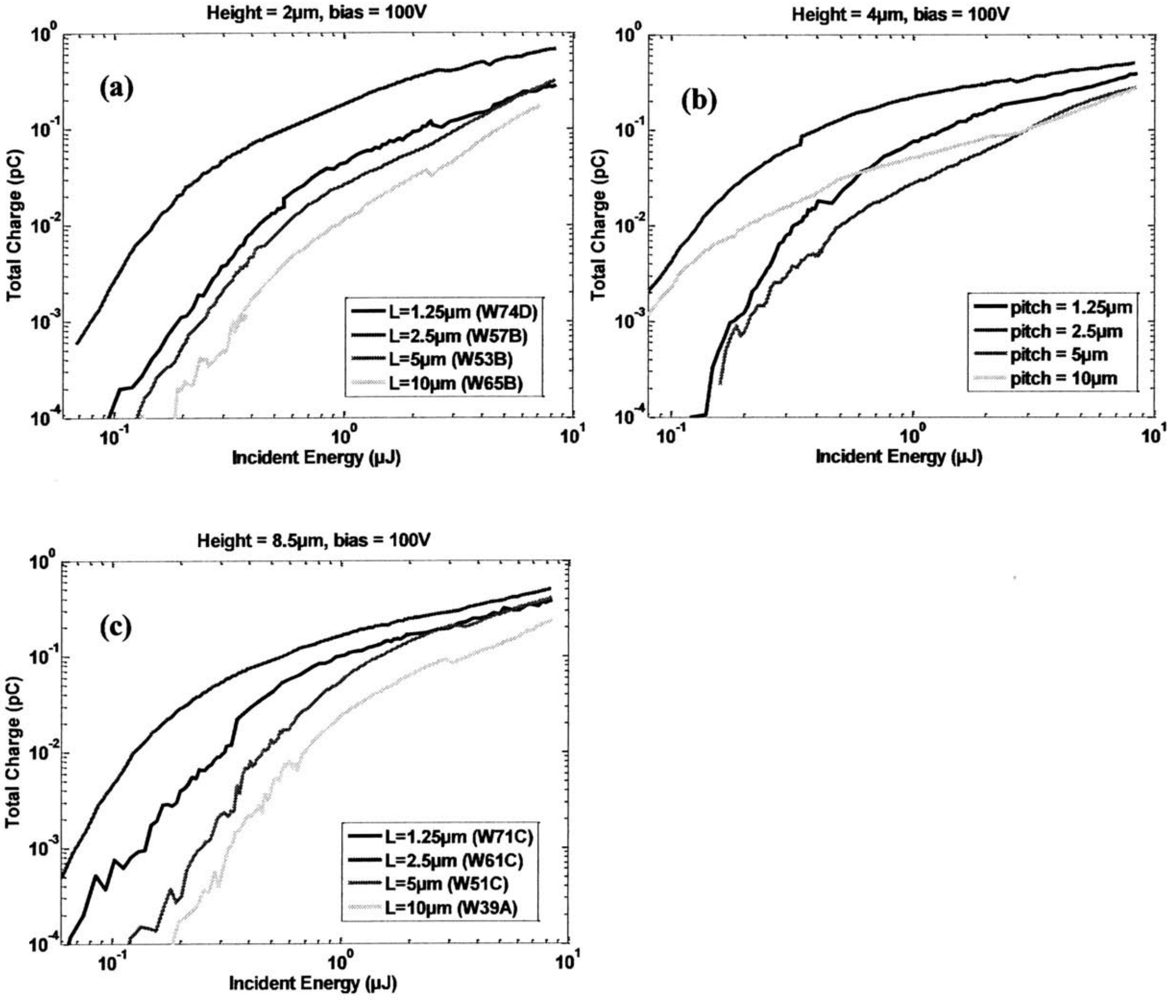

**Figure 25.** The plot of the charge-energy characteristics at various pitches of 1.25 µm, 2.5µm, 5µm and 10 µm given pillar heights of (a) 2µm, (b) 4 µm and (c) 8.5µm at the anode bias of 100V.

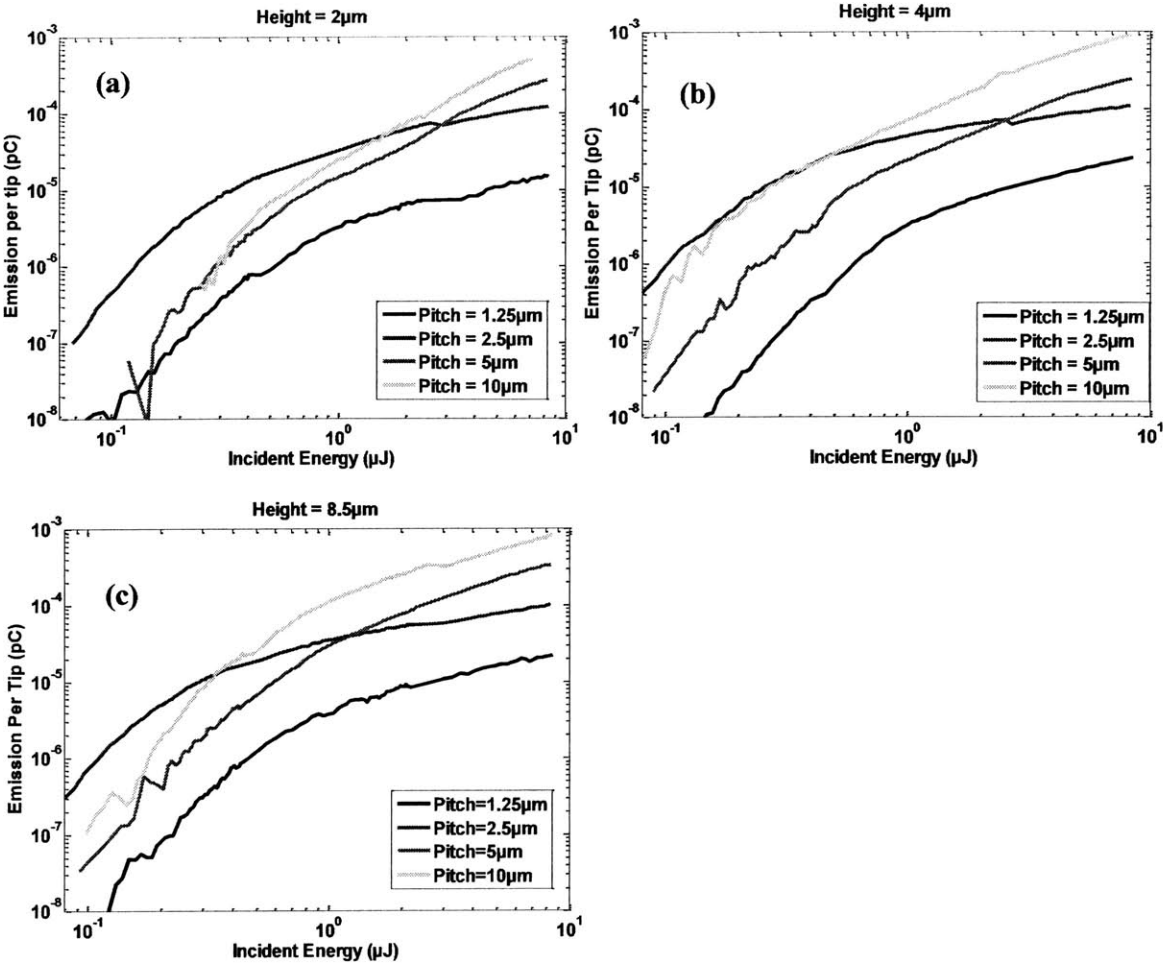

**Figure 26.** The plot of the charge emission per tip for various pitches of 1.25 µm, 2.5µm, 5µm and 10 µm after adjusting the number of tips at the heights of (a) 2 µm, (b) 4 µm, and (c) 8.5 µm at the anode bias of 1000V.

At the fixed incident energy, we studied how the charge emission varies with pitch scaling and the result is shown in Figure 27. Again, the device with 2.5 µm pitch has the highest emission. Figure 27 show a similar voltage dependence slope (~0.28) for all four emitter pitches and this slope is very close to the slope (~0.33) in [25]. The voltage dependence slope is smaller than 1 indicating that the emission is not fully space-charge limited due to the virtual cathode effect.

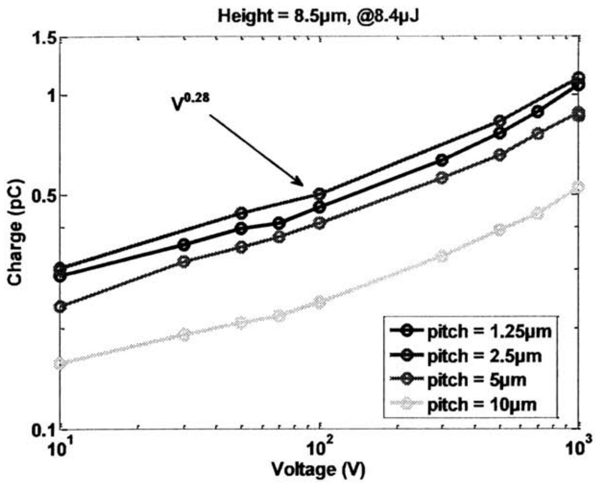

**Figure 27.** Charge emission vs. anode voltage between 10V and 1000V for devices with 8.5 μm pillar height and various pitches at the fixed incident energy of 8.4 μJ.

We are interested in studying the quantum efficiency (QE) of our devices as well. QE is a measurement of how efficient a device emits electrons when irradiated by incident photon of certain wavelength, and is usually measured as the number of electrons emitted per incident photon. Equation 6 calculates QE

$$QE = \frac{number\ of\ electrons}{number\ of\ photons} = \frac{total\ charge/q}{\frac{incident\ energy}{energy\ per\ photon}} \tag{6}$$

where $q$ is the elementary electric charge and the energy per photon with the wavelength of 800nm is 1.55 eV. By Equation 6, we obtain the plot of QE for various pitches at the heights of 2 μm, 4 μm and 8.5 μm. As shown in Figure 28 (a), (b) and (c), the QE first increases rapidly at low intensities (<~0.6 μJ), which corresponds to the 3-photon absorption process. At high intensities (or the strong field emission process, ~1 μJ), the QE saturates and becomes flat. For the pitches of 1.25 μm and 2.5 μm, the QE actually bends down after the flat regime. Recall that the virtual cathode effect is worse at the lower pitches (1.25 μm and 2.5 μm) as shown in Figure 23, so the bend-down of QE is due to the virtual cathode effect.

As shown in Figure 28, the overall QE does not exceed $10^{-6}$, which is high considering that only a very small fraction of the emitter surface is utilized, as the tip diameter is ~12 nm and the tip spacing is in order of microns. The emission is also greatly enhanced as compared to that of on planar Si, which has a QE of $10^{-10}$ [25]. The device with the pitch of 2.5 μm has the largest QE, which is another piece of evidence that there exists an optimum pitch with the best emission around 2.5 μm. At the fixed pitch of 2.5 μm, we observe that the height doesn't have a strong impact on the QE, as shown in Figure 28 (d), although the height of 4 μm yields the best QE.

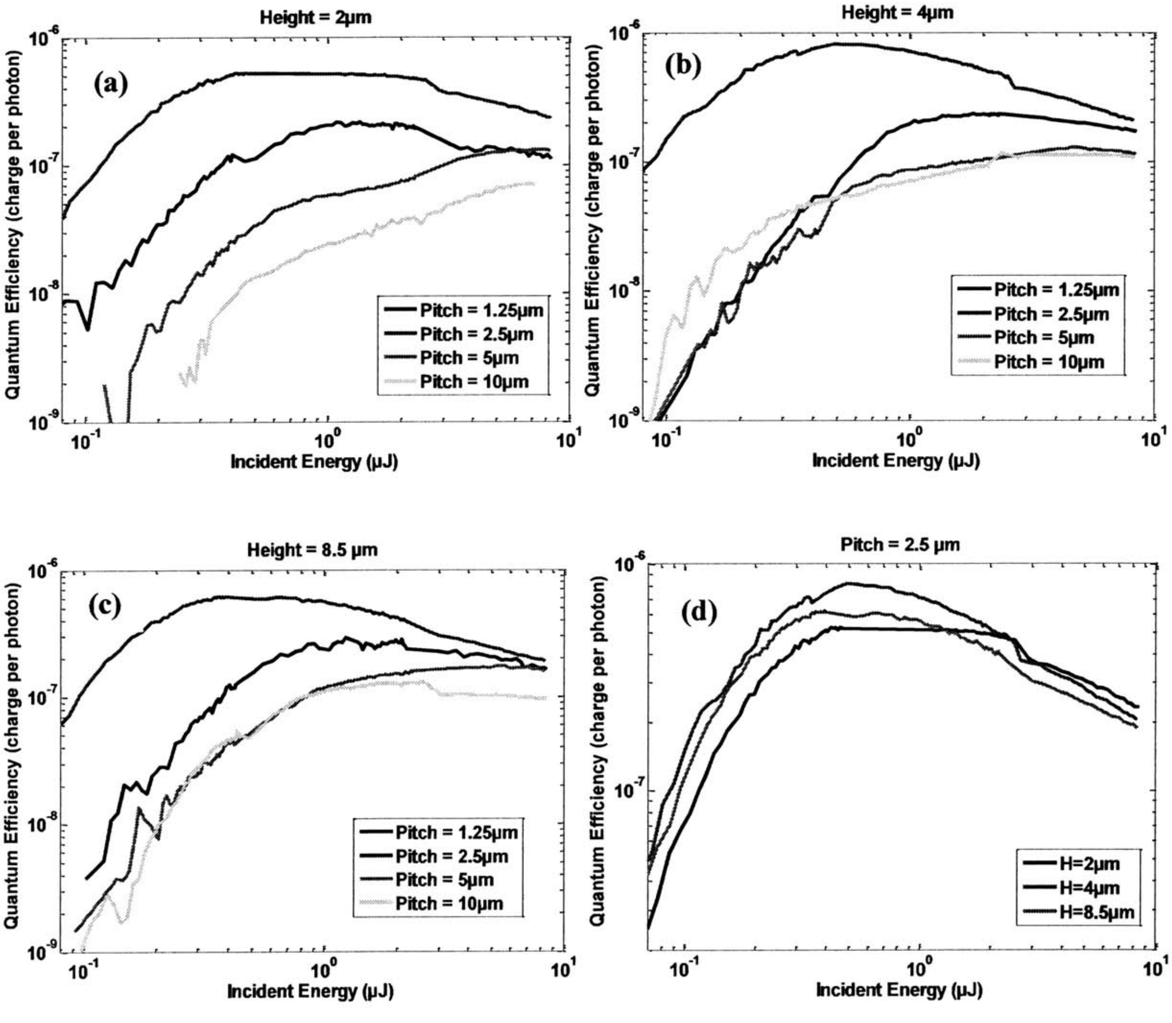

**Figure 28.** The plot of QE as a function of laser pulse energy for various pitches at the heights of (a) 2 μm, (b) 4 μm, (c) 8.5 μm, and (d) at the fixed pitch of 2.5 μm, the plot the QE vs. incident energy for different heights.

Based on the trends we have seen so far, the device with the best emission is the structure with 2.5 µm pitch. At the pitch of 2.5 µm, the height doesn't have a strong impact on the performance when the height is above 2 µm. To examine the stability of the performance of the device with the pitch of 2.5 µm, we expose this device on four different sample locations with four different combinations of incident energy and bias for 1800 seconds with the beam being unblocked at time 0s at an unexposed area. The emission is plotted as a function of time in Figure 29. All four curves show stable current emission after 8 million pulses, which is important for electron source applications to survive millions of cycles at high charge output [25]. The lowest curve has lower noise than the others. The highest curve shows an average 2.4 pC electron emission (7.2 nA of average current) at the incident energy of 9.5 µJ and the bias of 5000V.

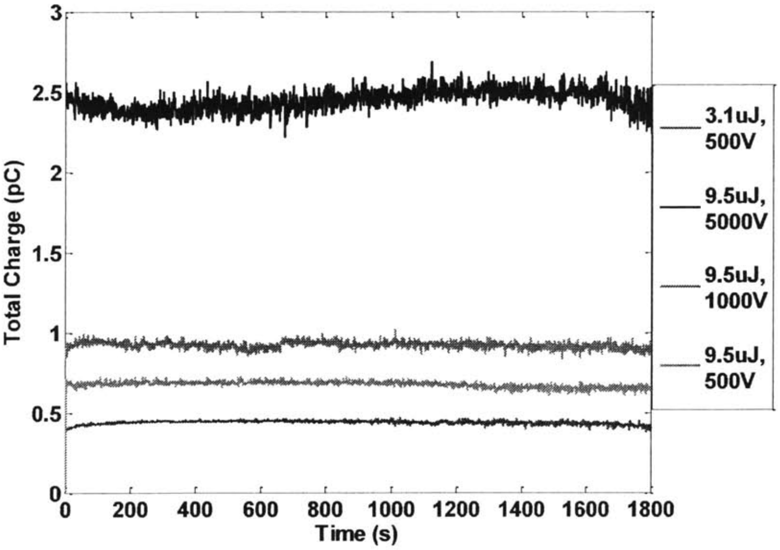

**Figure 29.** Current emission as a function of time. The device with 2.5 µm pitch and 8.5um height is exposed with four different combinations of incident energy and bias for 1800 seconds.

To demonstrate the effect of field enhancement on the tip emission, the charge yield is measured while rotating the polarization angle ($\theta$) at a fixed bias of 1000 V for the device with 2.5 µm pitch and 8.5 μm height. For low pulse energies (<~0.3 μJ), peak emission occurs when the polarization was along the axis of the tip, and minimum emission for the orthogonal polarization. The emission has a $\sin^6(\theta)$ dependence on the polarization and corresponds to the 3-photon absorption process [25]. In the case of high pulse energies, the polarization followed a $\sin^2(\theta)$ dependence, corresponding to the tunneling regime, but there is another mechanism which contributes to the second harmonic in Figure 30 (b). This mechanism has a $\cos^2(2\theta)$ fit which reverses the polarization (i.e. minimum along the axis of the tip, and maximum at the orthogonal polarization). This extra emission is due to the increase the surface area along the shank of the tips.

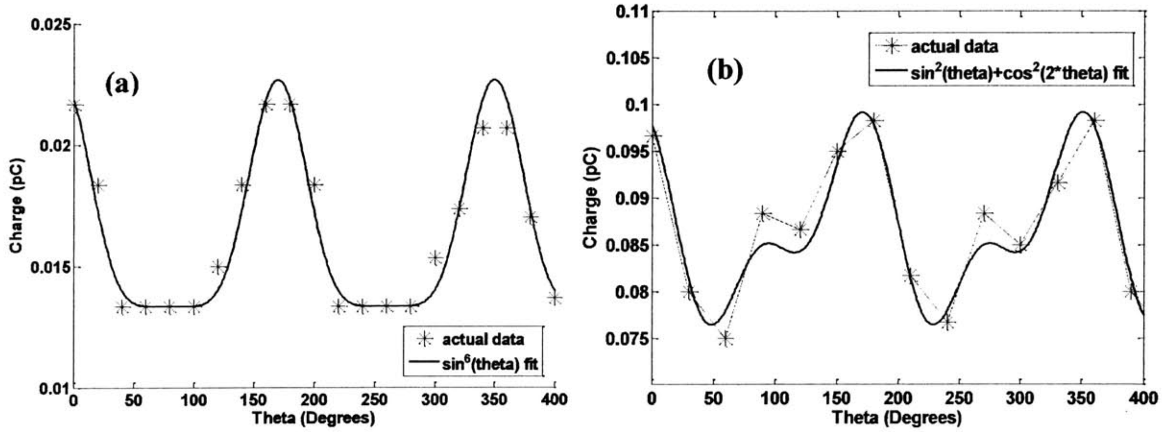

**Figure 30.** The charge yield as the function of the polarization angle (*θ*) at (a) low pulse energy (0.3 μJ), and (b) high pulse energy (0.7 μJ).

# Chapter 7. Summary and Future Work

We used simulations to explore how the geometry and the morphology affect the emission of the photocathode emitter arrays. Based on 2D simulations, we have seen several trends. First, the field factor has a negative power dependence factor on the tip radius (i.e. the field factor is a strictly decreasing function of the tip radius). Second, the electric field is strictly increasing with respect to the pitch; moreover, it is enhanced rapidly in the low-pitch region and saturates in the high-pitch region. The relationship between the field factor and the pitch at the constant height can be modeled by an exponential decay fit. Third, the field factor is strictly increasing with respect to the pitch with a diminishing return. Similarly, the relationship between the saturated field factor and the height can be modeled by an exponential decay fit as well. Fourth, we extracted a table of pitch to height ratio for different percentage of saturation level. For example, if we want to achieve 99% of the saturated field factor, we need to make the pitch about 46 times the emitter height.

We also characterize the devices, especially their charge-energy characteristics. We observe that the emission process has two main processes: the 3-photon absorption process and the strong field or tunneling process. We also observe the formation of a virtual cathode at high charge emission yields and the virtual cathode effect is worse for low pitch. Our experimental result agrees with the simulation result. For instance, Figure 23 (d) is a strong piece of evidence that the field factor is strictly increasing with respect to the height but with a diminishing return. Another important finding is that there exists an optimum pitch with the highest emission around 2.5 μm, due to the trade-off between the field enhancement at the tip and the number of emitters. At the pitch of 2.5 μm, devices with heights of 2 μm, 4 μm and 8.5 μm all have similar emission, although the device with the height of 4 μm resulted in a slightly larger QE. Therefore, we conclude that the device with the highest emission is the one with the pitch of 2.5 μm and the height ≥ 2 μm.

In the future, we could expand this work in several ways. Due to the constraint of the computation ability of MTL servers, we could only simulate 2D models even though 3D models are more accurate. Therefore, it would be advantageous to use 3D models to extract the exact the field factor. Also, the simulation shows that the device with the height of only 0.2 μm still can achieve a field factor of ~2.4. Therefore, it will be interesting to fabricate devices with shorter pillars (below 2 μm) and to see whether it still produces satisfactory performance.

Also, we have seen from the experimental result that the current best device with the highest emission is the one with 2.5 μm pitch and ≥2 μm tall. However, it doesn't necessary mean that the optimum pitch is 2.5 μm. It will be interesting to fabricate devices with pitches that is less than and greater than 2.5 μm (such as 2 μm and 3 μm) so we know where the true optimum pitch is.

Both the simulation and device characterization ignore how much momentum the electron carries when it is emitted from the tip. We can perform a time of flight (TOF) electron spectrometer, which measures the longitudinal electron energy spectrum as a function of pulse energy. It will be interesting to see how the emitted electrons' energies spread on the energy spectrum for devices with different pitches, and how it compares to previous work reported in the literature [25].

## Reference

[1] P. Dombi, A. Hörl, P. Rácz, I. Márton, A. Trügler, J. R. Krenn, and U. Hohenester, "Ultrafast Strong-Field Photoemission from Plasmonic Nanoparticles," *Nano Lett.*, vol. 13, no. 2, pp. 674–678, Feb. 2013.

[2] W. S. Graves, F. X. Kärtner, D. E. Moncton, and P. Piot, "Intense superradiant X rays from a compact source using a nanocathode array and emittance exchange," *Phys. Rev. Lett.*, vol. 108, no. 26, p. 263904, Jun. 2012.

[3] B. Barwick, D. J. Flannigan, and A. H. Zewail, "Photon-induced near-field electron microscopy," *Nature*, vol. 462, no. 7275, pp. 902–906, Dec. 2009.

[4] P. D. Keathley, W. P. Putnam, A. Sell, S. Guerrera, L. F. Velásquez-García, and F. X. Kaertner, "Laser Induced Annealing Dynamics of Photo-Electron Spectra from Silicon Field Emitter Arrays", *LEO Sci. Innov.*, *CM4L.7*, May 2012.

[5] C. Ropers, D. R. Solli, C. P. Schulz, C. Lienau, and T. Elsaesser, "Localized Multiphoton Emission of Femtosecond Electron Pulses from Metal Nanotips", *Phys. Rev. Lett.*, Vol. 98, pp. 043907, 2007.

[6] P. Hommelhoff, Y. Sortais, A. Aghajani-Talesh, and M. A. Kasevich, "Field Emission Tip as a Nanometer Source of Free Electron Femtosecond Pulses", *Phys. Rev. Lett.*, Vol. 96, pp. 077401, 2006.

[7] M. Krüger, M. Schenk and P. Hommelhoff, "Attosecond control of electrons emitted from a nanoscale metal tip", *Nature,* vol. 475, pp. 78–81, 2011.

[8] R. Bormann, M. Gulde, A. Weismann, S. V. Yalunin, and C. Ropers, "Tip-Enhanced Strong-Field Photoemission", *Phys. Rev. Lett.*, vol. 105, pp. 147601, 2010.

[9] P. Dombi, et al., "Ultrafast Strong-Field Photoemission from Plasmonic Nanoparticles". *Nano Lett.*, vol. 13, pp. 674–678, 2013.

[10] G. Herink, D. R. Solli, M. Gulde, and C. Ropers, "Field-driven photoemission from nanostructures quenches the quiver motion", *Nature*, vol. 483, pp. 190–193, 2012.

[11] K. L. Jensen, Y. Y. Lau and D. McGregor, "Photon assisted field emission from a silicon emitter", *Solid-State Electronics*, vol. 45, pp. 831-840, 2001.

[12] L. Liao, H. B. Lu, M. Shuai, J. C. Li, Y. L. Liu, Liu, Z. X. Shen, and T. Yu, "A novel gas sensor based on field ionization from ZnO nanowires: moderate working voltage and high stability," *Nanotechnology*, vol. 19, no. 17, Mar 2008.

[13] L. Y. Chen, "Double-gated Isolated Vertically Aligned Carbon Nanofiber Field Emission and Field Ionization Arrays," PhD Thesis, MIT, 2007.

[14] R. Gomer, *Field Emission and Field Ionization*, Harvard University Press, 1961.

[15] M. E. Swanwick, P. D. Keathley, F. X. Kartner, L. F. Velásquez-García, "Nanostructured silicon photo-cathodes for x-ray generation," *Vacuum Nanoelectronics Conference (IVNC)*, 2013 26th International, pp.1,2, 8-12, July 2013.

[16] "Introduction to Comsol Multiphysics", COMSOL, acessed online, pp. 34, 44., 2014. http://www.comsol.com/model/download/186405/models.rf.parabolic_reflector.pdf.

[17] M. E. Swanwick, P. D. Keathley, F. X. Kartner, L. F. Velásquez-García, "Ultrafast photo-triggered field emission cathodes using massive, uniform array of nano-sharp high-aspect-ratio

silicon structures," *17th International Conference on Solid-State Sensors*, Actuators and Microsystems, p. 2680–2683, 2013.

[18] "Parabolic Reflector Antenna," COMSOL, acessed online, pp. 2, 2014. http://www.comsol.com/model/download/186405/models.rf.parabolic_reflector.pdf.

[19] G.E.M. Jauncey, "The scattering of x-ray and Bragg's law", *Proceedings of the National Academy of Sciences*, vol.10, no.2, pp.57-60, 1924.

[20] "Bragg's law", Wikipedia, accessed online, 2014. http://en.wikipedia.org/wiki/Bragg's_law.

[21] Susan C. Hagness, Allen Taflove, Stephen D. Gedney, "Finite-Difference Time Domain Methods", *Handbook of Numerical Analysis*, Elsevir B. V., 2005

[22] R. Bormann, M. Gulde, A. Weismann, S. V. Yalunin, and C. Ropers, "Tip-Enhanced Strong-Field Photoemission," *Phys. Rev. Lett.*, vol. 105, p. 147601, 2010.

[23] L. V. Keldysh, *Sov. Phys. JETP*, vol. 20, p. 1307−1314, 1965.

[24] S. V. Yalunin, M. Gulde, and C. Ropers, "Strong-field photoemission from surfaces: Theoretical approaches," *Phys. Rev. B,* vol. 84, no. 195426, 2011.

[25] M. E. Swanwick, P. D. Keathley, A. Fallahi, P. R. Krogen, G. Laurent, J. Moses, F. X. Kartner, and L. F. Velásquez-García, "Nanostructured Ultrafast Silicon-Tip Optical Field-Emitter Arrays," *Nano Letters*, 2014, DOI 10.1021.

[26] Á.Valfells1, D. W. Feldman, M. Virgo, P. G. O'Sheal and Y. Y. Lau, " Effects of pulse-length and emitter area on virtual cathode formation in electron guns," *Phys. Plasmas 1994-Present*, vol. 9, p. 2377–2382, 2002.